2014

TUNING, AVO, AND FLAT-SPOT EFFECTS IN A SEISMIC ANALYSIS OF NORTH SEA BLOCK F3

Qiang Guo
Michigan Technological University

TUNING, AVO, AND FLAT-SPOT EFFECTS IN A SEISMIC ANALYSIS OF NORTH SEA BLOCK F3

By
Qiang Guo

A THESIS

Submitted in partial fulfillment of the requirements for the degree of
MASTER OF SCIENCE
In Geophysics

MICHIGAN TECHNOLOGICAL UNIVERSITY
2014

This thesis has been approved in partial fulfillment of the requirements for the Degree of MASTER OF SCIENCE in Geophysics.

Department of Geological/Mining Engineering and Sciences

Thesis Advisor: *Dr. Wayne D. Pennington*

Committee Member: *Dr. Roger M. Turpening*

Committee Member: *Dr. Gregory P. Waite*

Committee Member: *Dr. Zhen Liu*

Department Chair: *Dr. John S. Gierke*

Table of Contents

Acknowledgement

My deepest appreciation goes to Dr. Wayne D. Pennington, for his kind advice, warm encouragement, and the confidence he has given me throughout my graduate research. Without his patient and persistent help this thesis would not have been possible.

I would also like to express my sincerest gratitude to my committee members Dr. Roger M. Turpening, Dr. Gregory P. Waite and Dr. Zhen Liu, for their helpful guidance and suggestions.

I want to show my special thanks to my fellows, in particular Nayyer Islam, I had greatly benefited from working with you, and appreciate the help and advices you give me during my research. Also thank you, Yeliz Egemen and Lu Yang, I appreciate your support, and will always remember the courses and projects we had worked on and discussed with together. In addition, I also want to express my appreciation to Dr. Wen Xiaotao and Dr. Zhang Bo, for their kind help and suggestions on my thesis.

I want to thank the OpendTect (dGB Earth Sciences) who provided the data of the F3 Block and the software for me to display and analyze. I want to thank the CREWES at University of Calgary, who created the Matlab codes for AVO analysis.

The last but the most important, I want to express my heartfelt appreciation to my parents, Xindong Guo and Yuping Wu, and my girlfriend, Chunhui Zhang. Without your love, support and understanding, I couldn't be able to get my work done. I love you and bless you forever.

Abstract

Reflection seismic data from the F3 block in the Dutch North Sea exhibits many large-amplitude reflections at shallow horizons, typically categorized as “brightspots ” (Schroot and Schuttenhelm, 2003), mainly because of their bright appearance. In most cases, these bright reflections show a significant “flatness” contrasting with local structural trends.

While flatspots are often easily identified in thick reservoirs, we have often occasionally observed apparent flatspot tuning effects at fluid contacts near reservoir edges and in thin reservoir beds, while only poorly understanding them. We conclude that many of the shallow large-amplitude reflections in block F3 are dominated by flatspots, and we investigate the thin-bed tuning effects that such flatspots cause as they interact with the reflection from the reservoir’s upper boundary. There are two possible effects to be considered: (1) the “wedge-model” tuning effects of the flatspot and overlying brightspots, dimspots, or polarity-reversals; and (2) the stacking effects that result from possible inclusion of post-critical flatspot reflections in these shallow sands. We modeled the effects of these two phenomena for the particular stratigraphic sequence in block F3. Our results suggest that stacking of post-critical flatspot reflections can cause similar large-amplitude but flat reflections, in some cases even causing an interface expected to produce a ‘dimspot’ to appear as a ‘brightspot’.

Analysis of NMO stretch and muting shows the likely exclusion of critical offset data in stacked output. If post-critical reflections are included in stacking, unusual results will be observed. In the North Sea case, we conclude the tuning effect was the primary reason causing for the brightness and flatness of these reflections. However, it is still important to note that care should be taken while applying muting on reflections with wide range of incidence angles and the inclusion of critical offset data may cause some spurious features in the stacked section.

1. Introduction: Observations and Statement of Problem

Direct hydrocarbon indicators (Appendix A) have long assisted in the success of exploration projects. Brightspots, which demonstrate an increase in (negative) reflection coefficients as a water sand transitions to a gas or light-oil sand beneath a higher-impedance cap rock, are easy to recognize and often are exploited because of their prominence in a seismic section, and flatspots are easy to recognize because of their unconformable flatness, and are always positive in sign. Brown (2012) has emphasized that overlooked exploration targets include 'dimspots' that are often difficult to identify because of their low amplitude and lack of contrast with the surrounding rocks; tracking of prominent (positive) reflections over the flanking water sand may follow the flatspot rather than the dimmed reservoir top. Polarity reversals exist where the overlying shale is of higher acoustic impedance than the hydrocarbon sand, yet lower impedance than the water sand; these are presumably difficult to recognize for the same reasons as dimspots.

We present an interesting case from the F3 Block of the offshore Netherlands. The area exhibits significant bright reflections that are very flat in nature and which contrast with the structural trend of the surrounding rocks. The data set used for this work was provided by OpendTect (dGb Earth Sciences), and includes post-stack 3D seismic data with limited well-log data from four different wells drilled in the same region but targeting deeper horizons. The data set also demonstrates excellent examples of gas chimneys, direct hydrocarbon indicators, and stratigraphic features. Of interest in our study are small shallow uneconomic reservoirs that exhibit very bright and flat reflections. Figure 1.1 shows one example of those reservoirs. Throughout this paper, we will focus on this specific reservoir, considering it a representation of the same phenomenon in other nearby reservoirs. Note the brightness of the reservoir reflection marking the top of the reservoir. It is this bright nature of these reflections that has led to their categorization as 'brightspots' in the literature (Schroot and Schuttenhelm, 2003).

In order to estimate the departure of this reflection from structural trend, we compared it with immediately overlying layers. The green line in Figure 1.1 shows a tracked horizon,

giving an indication of the structural trend. A phantom horizon (tracked horizon that is shifted in an appropriate time) was created from this, and is displayed in blue color below the tracked horizon. Although this phantom horizon is conformable with the flanking water sand reflections, note that it is not conformable with the bright reflections associated with the gas reservoir. This observation suggests that the "red" reflections (negative, indicating an acoustic impedance decrease), are not simple brightspots but are influenced by the underlying flatspot. Both the flatness and the brightness of the reservoir reflections need to be explained if we are to properly interpret similar features elsewhere.

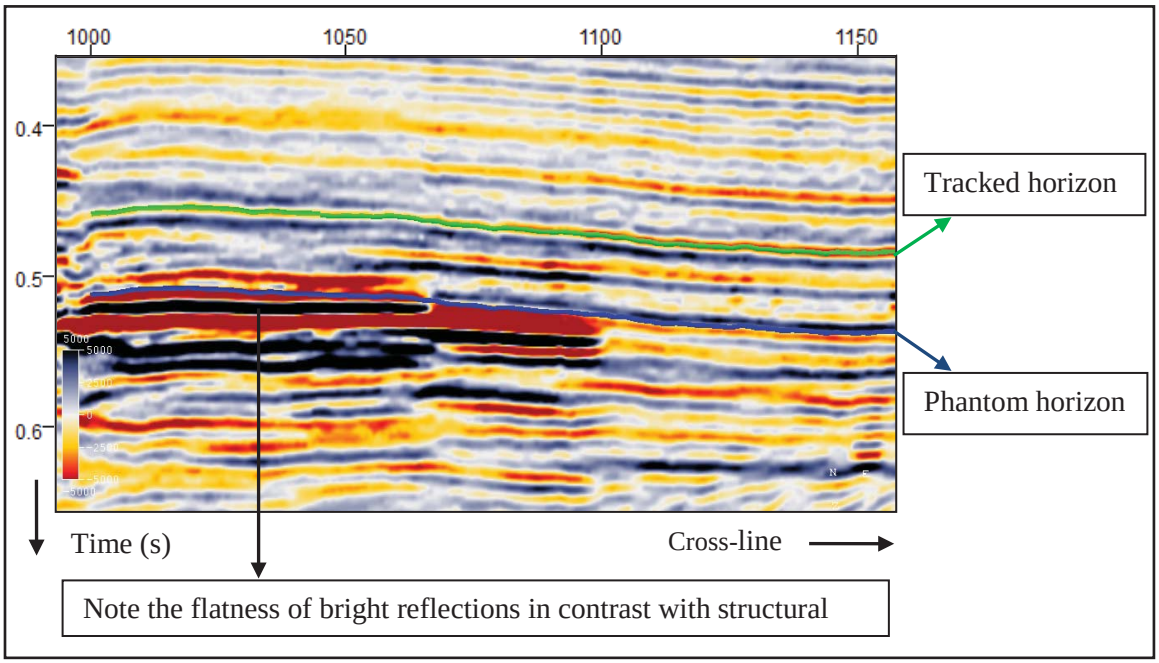

Figure 1.1. One of the many shallow reservoirs from the F3 Block (Inline230). Reflections associated with the reservoir are flat compared to the local structure, indicated by a tracked horizon in green and a phantom horizon created from it, in blue. The figure includes roughly 200m horizontally and 300ms on the vertical axis. Red indicates a decrease in impedance; black an increase.

In order to examine these features, we created synthetic data from different models. We examined tuning effects for normal incidence on thin beds, and we examined non-normal incidence pre-stack post-critical phase delays and their effects on stacking.

These shallow layers consist of alternating thin beds of shale and sand. Tuning effects are often a problem in such beds; Ricker (1953), Widess (1973), Kallweit et al. (1982) and Chopra et al. (2006), and others have studied tuning effects in details and have established tuning thicknesses and limits of resolution. The reservoirs under discussion exhibit features that suggested to us that tuning plays an important role in the generation of these flat reflections. We expected this tuning to arise from the reflections from the top of the reservoir and from the gas water contact (GWC). First, we examine this issue from a normal incidence assumption, as do most thin-bed studies.

The effect of post-critical reflections is usually not considered for stacking purposes. But these reservoirs lie at very shallow depths (~500m), and it is likely that post-critical reflections have been recorded; these post-critical reflections may or may not have been muted prior to stacking. Post-critical reflections involve a phase shift, and if stacked in will change the wave shape and amplitude of the final stacked event. In addition, because these rocks are highly unconsolidated, and the elastic properties of the rocks will be strongly influenced by the nature of pore fluid (e.g., Hilterman, 2001), we may expect to observe a large velocity contrast at the GWC. This, in turn, will result in a small critical angle and correspondingly short offset to the critical distance. Taken together, we are correct to concern ourselves with the possibility that shallow stacked reflections may be contaminated by the post-critical reflections, and therefore we include the effect of post-critical reflections in our study.

As we do not know the stacking range that was used for this particular dataset, analysis about NMO stretch and muting was performed to estimate the possible NMO stretch for different offsets, based on established industry standards. A simple layered earth model was assumed to overly the reservoir in order to generate synthetic pre-stack seismograms at reasonable offset ranges, and one NMO stretch and muting criterion was adopted here. We use these observations to draw conclusions about the likelihood of incorporating post-critical reflections in the stacked results in Block F3, but the general caveats that result may be of interest anywhere.

The work involved four basic steps. At the first stage we performed rock-physics modeling to estimate the unknown formation properties needed for analysis. The second step was to conduct forward seismic (normal incidence) modeling to study possible tuning effects, and the third step involved AVO analysis and effect of post-critical reflections. Finally, NMO stretch and muting were estimated for this data set, suggesting whether or not post-critical offsets were stacked in. The results from all these modeling methods were then assembled to guide our conclusions.

2. Tuning Effects

2.1. Tuning Effects for Normal Incidence

Ricker (1953), Widess (1973), Kallweit et al. (1982) and Chopra et al. (2006) have studied the tuning effect in detail and have established tuning thicknesses and resolvable limits. These are briefly reviewed in the following section.

Widess (1973) concluded that for bed thickness thinner than the half of the wavelength ($\lambda/2$, where λ is the dominant wavelength), the reflections from the top and bottom of the layer interfere in ways that change the shape and amplitude of the wavelet. As the bed thins to one fourth of the wavelength ($\lambda/4$), the amplitude of the wavelet grows and reaches a maximum, through the constructive interference of the side and main lobes of the wavelet. This thickness is termed as the "tuning thickness". When the bed thickness reaches one eighth of a wavelength ($\lambda/8$), the composite wavelet resembles a derivative of the original waveform, and no change in trough-to-peak time will be observed; the amplitude then decreases toward zero as the bed continues to thin (Widess, 1973; Kallweit and Wood, 1982). Widess (1973) pointed out that a thin-bed thickness should be at least $1/8^{th}$ of dominant wavelength in order to be delineated. However, in the presence of noise, the resolution is usually taken to be $\lambda/4$ (Chopra and Castagna, 2006).

In order to demonstrate the conclusions previous authors have made and to confirm our modeling approach, we generated a wedge model using a dipping upper layer above a flat interface with an opposite but equal reflection coefficient (RC). Figure 2.1a shows the seismic section that is generated by convolving a 50Hz Ricker wavelets with such a wedge model, tapering from 25ms to 0ms in time-thickness. Figure 2.1b shows the change of amplitude (blue line) of each reflection and of the composite wavelet where tuning occurs, and it shows the trough-to-peak time (green line), both as function of bed thickness. The behavior of these tuning wavelets is similar to that shown by Widess (1973).

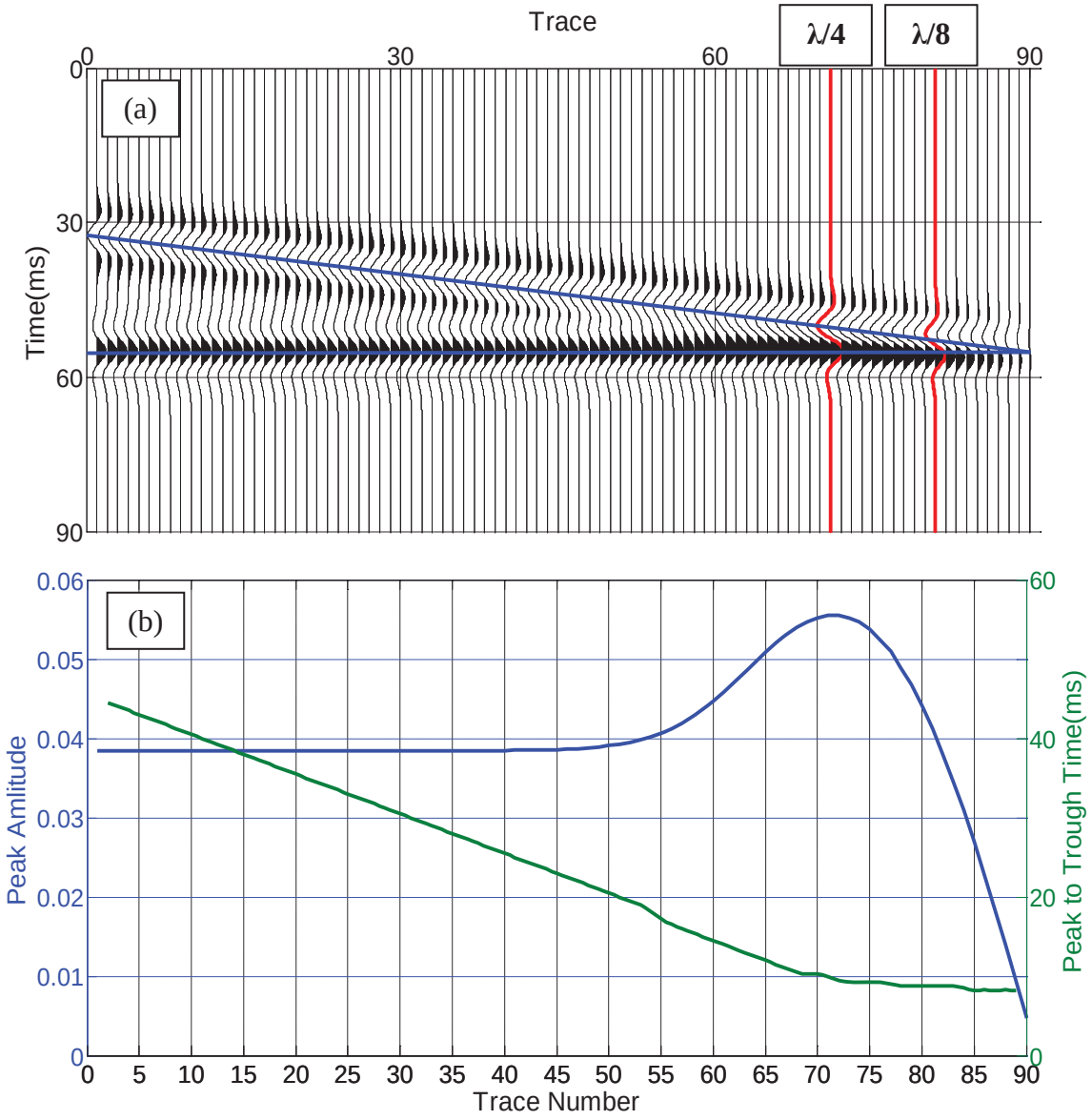

Figure 2.1. Wedge model analysis showing the tuning effect in detail. (a) Synthetic wedge model (indicated by the blue lines), with reflection coefficients that are negative at the dipping upper interface and positive at the lower flat interface, convolved with a 50Hz Ricker wavelet; (b) Amplitude (blue line) and trough-to-peak time (green line) of the composite wavelet as a function of bed thickness.

When a gas or oil layer is very thin, this tuning could occur between the flatspot reflection generated by the GWC or OWC (gas-oil contact or oil-water contact) and the overlying interface; in the model presented in Figure 2.1, this overlying reflection was assumed to be of equal and opposite amplitude, resembling a strong brightspot. Many of

the published examples of tuning employ models in which the overlying and underlying rocks are identical (and often assumed to be shale), and the wedge in between represents the potential reservoir rock (often assumed to be a sand).

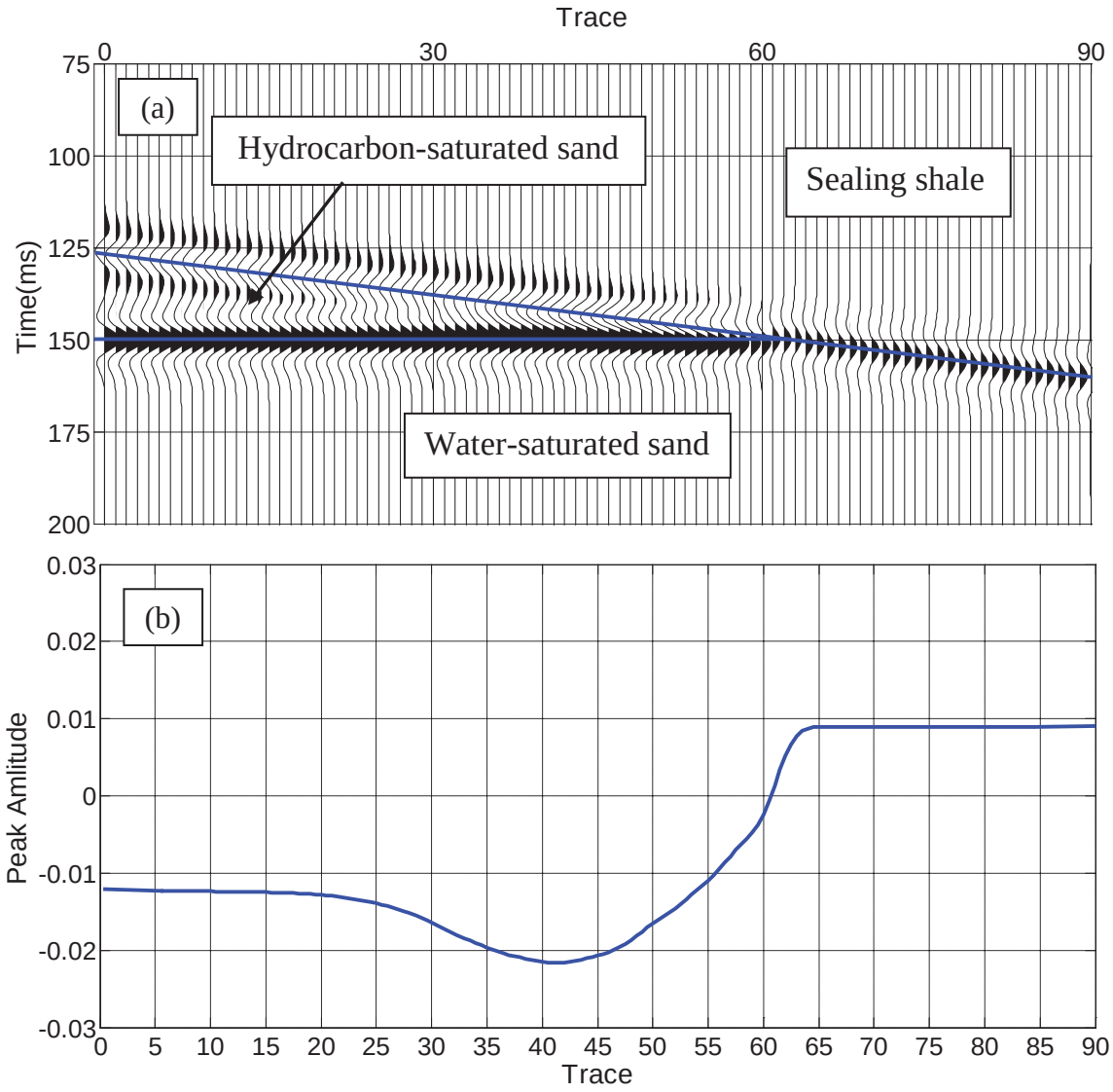

Figure 2.2. The model results showing the intriguing reflection-tuning patterns. (a) The normal-incidence responses for the structural model we are interested in, in which a wedge of hydrocarbon-saturated rock is overlain by sealing shale and underlain by water-saturated rock (interfaces are indicated by blue lines). We use a polarity reversal case in this example; (b) Amplitude of the reflection from the dipping interface, where a bright reflection occurs over the hydrocarbon-saturated rock and dim reflections over the water-saturated rock. Notice the change of amplitude due to the tuning and the sign change of the reflection indicating the polarity reversal at the termination of the hydrocarbon wedge.

In these cases, the reflection coefficients are identical but have opposite polarity. Some published examples (e.g., Robertson et al., 1984) use reflection coefficients that are identical in both amplitude and polarity above and below the wedge. In our case, we are interested in a wedge of hydrocarbon-saturated rock overlain by a sealing formation and underlain by a water-saturated rock that is otherwise similar to that in the wedge; in addition, the flank of the wedge continues to dip as the sealing formation directly overlies the water-saturated rock. The results of this model are provided in Figure 2.2 showing some intriguing reflection-tuning patterns. But it is also important to include the effects of non-normal angles of incidence in order to better understand the stacked response; this is covered in the following section.

2.2. Tuning Effects for Amplitude Variation with Offset

The analysis of amplitude variation with offset (AVO, details presented in Appendix B) was a significant component in the development of DHIs, and AVO techniques are identified by Hilterman (2001) as the second era of amplitude interpretation, following the brightspot era.

Ostrander (1984) initially established the relationship between AVO characteristics with lithological identification and verified the use of AVO for seismic interpretation for gas sands. Rutherford and Williams (1989) grouped AVO responses into three classes based on normal incident reflection coefficient and AVO behavior. Castagna et al. (1998) added an additional Class IV. Figure 2.3 shows the four classic AVO classifications for a typical shale-gas sand interface. Some other authors have identified additional "classes" but most authors refer only to these four; it should be recognized that AVO behavior can display other characteristics, but these four classes are the ones generally discussed.

For most brightspots associated with low-impedance sands overlain by high-impedance shales, Class III AVO behavior is observed; that is, they exhibit a negative reflection at zero offset (R_o) and with increasing (negative) amplitude with increasing offset. For most dimspots associated with high-impedance sands overlain by low-impedance shales, Class

I (or II) AVO characteristics are observed, with positive R_o and decreasing positive or perhaps increasingly negative amplitude with increasing offset; because the dimspot classification is based on stacked images, the stack must still be positive. All flatspots exhibit similar behavior, in which the reflection is always positive and increasing with offset; this is because the effect of fluid substitution in a given reservoir rock will always result in low acoustic impedance (hydrocarbon zone) over high acoustic impedance (water zone), with negligible changes in shear velocity across the interface. Note that in most classification systems, this is not recognized as a distinct class; we have added a curve demonstrating this behavior to Figure 2.3.

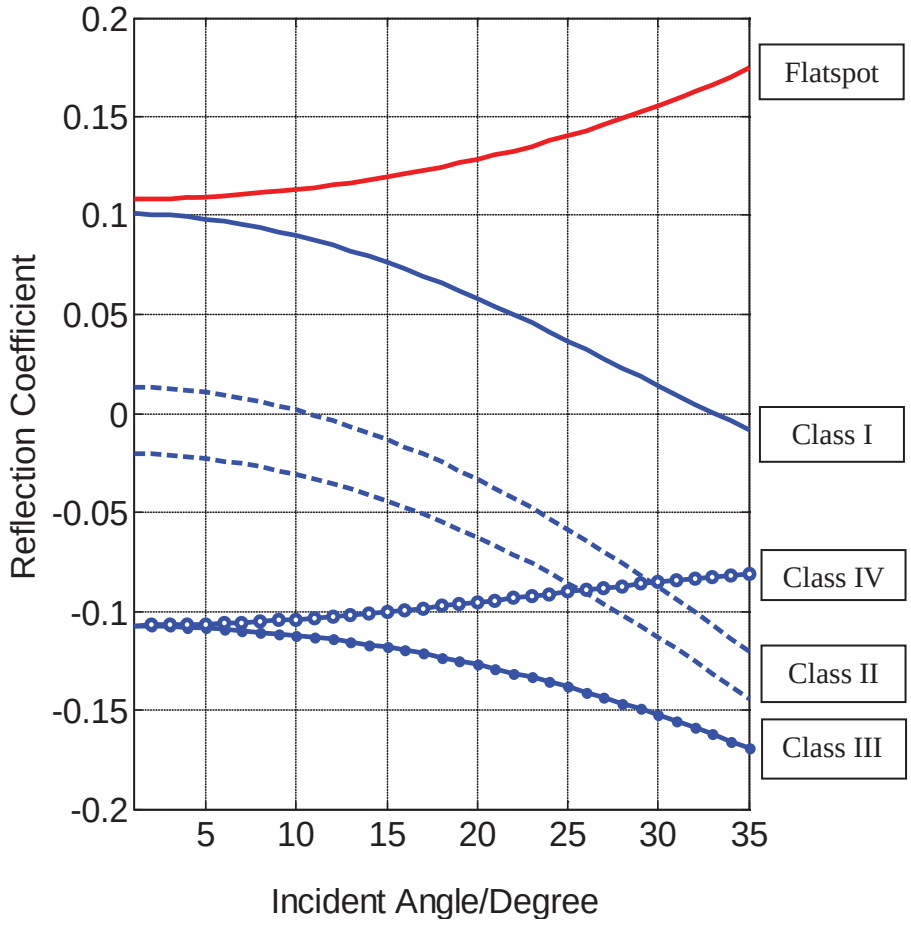

Figure 2.3. The four usual AVO classifications defined by Rutherford, et al. (1989) and Castagna, et al. (1998), and typical flatspot behavior.

Having established that inclusion of AVO effects is important, even for stacked data (we will later refer to examples in Figure 3.9, where stacking over different angle ranges yields different stacked outputs), we also need to consider the effects of normal-moveout correction and stacking, which tend to distort the wavelet.

2.3. NMO Correction, Stretch and Muting

The amount of extra travel time (Δt_{nmo}) for reflections observed at non-zero offset, due to obliquity of path compared to the normal-incidence trace, is called Normal Move-Out (NMO), and can be readily observed and computed (Buchholtz, 1972). In conventional processing, CMP gathers are corrected for NMO and stacked into single, stacked, traces in which multiples and other noise components are greatly reduced. It is commonly, although incorrectly, assumed that the stacked trace can be treated as if it were a high-quality normal-incidence trace; the error comes primarily in ignoring the changing amplitude contributions that come from offset traces.

However, the conventional NMO correction (Appendix C) uses different values of Δt_{nmo} at different times, and this can result in different values within the wavelet itself. This is most pronounced for early times and long offsets, and can lead to a significant reduction in high frequency content of the wavelet (Andrew et al., 2000). Buchholtz (1972) analyzed wavelet distortion due to NMO correction and pointed out the most severe stretching of the wavelet occurs at the intersections of reflection hyperbolae. Dunkin and Levin (1973) concluded that conventional NMO correction stretches the wavelet such that its spectrum is linearly compressed and multiplied by a factor defined by offset and the stacking or NMO velocity used (V_{nmo}). It can be referred to the example in Figure 3.11, notice that the NMO-corrected wavelets in Figure 3.11b have lower frequency content than these before correction in Figure 3.11a, and these distortions are pronounced for shallow and far-offset reflections.

The usual solution for the NMO stretch problem is simply to discard or mute the severely stretched part of the traces, dependent on time and offset (Buchholtz, 1972). One criterion

for offset-and-time-dependent muting is the percent change in frequency caused by the NMO stretch, given by Equation (2.1) and due to Yilmaz (1987) (derived in Appendix C).

$$\frac{\Delta f}{f} = \frac{\Delta t_{NMO}}{t_o} \qquad \text{Equation 2.1}$$

Here f is the dominant frequency of wavelet before NMO correction; Δf is the change in frequency after NMO correction, t_o is the two-way reflection time at zero offset, and Δt_{NMO} is derived from the Dix equation (Dix, 1955) (see also Appendix C). Usually a stretch limit of 50% is taken to determine the muting zone of the CMP gather. Sometimes this limit may extend to 100% based on how much far-offset information is desired in the stack.

The established industry NMO muting criterion described above will be used to determine the chance of muting within or without supercritical offset for our dataset, demonstrating an effect that may or may not contribute to other datasets.

3. Methodology and Application to the Dipping-Sand Model

3.1. Rock-Physics Modeling

3.1.1. Rock Properties

The location of the target reservoir is Inline 210-250, Crossline 1050-1200 at a depth of 520-560 ms in the data provided from F3 Block of North Sea. None of the four wells drilled in the block penetrated the reservoir but a nearby well (F03-4) provides data for the water-saturated equivalent sand as well as for the overlying shale. Figure 3.1a shows the well location and water-saturated sand with respect to the reservoir.

This well has only gamma-ray and sonic logs at this depth. The sonic velocities for overlying shale and wet-sand as noted from the well-logs (Figure 3.1b) are listed in Table 3.1. We also used standard relationships to estimate other important properties (fluid and grain properties), and the parameters for the upcoming rock-physics modeling are given in Table 3.1.

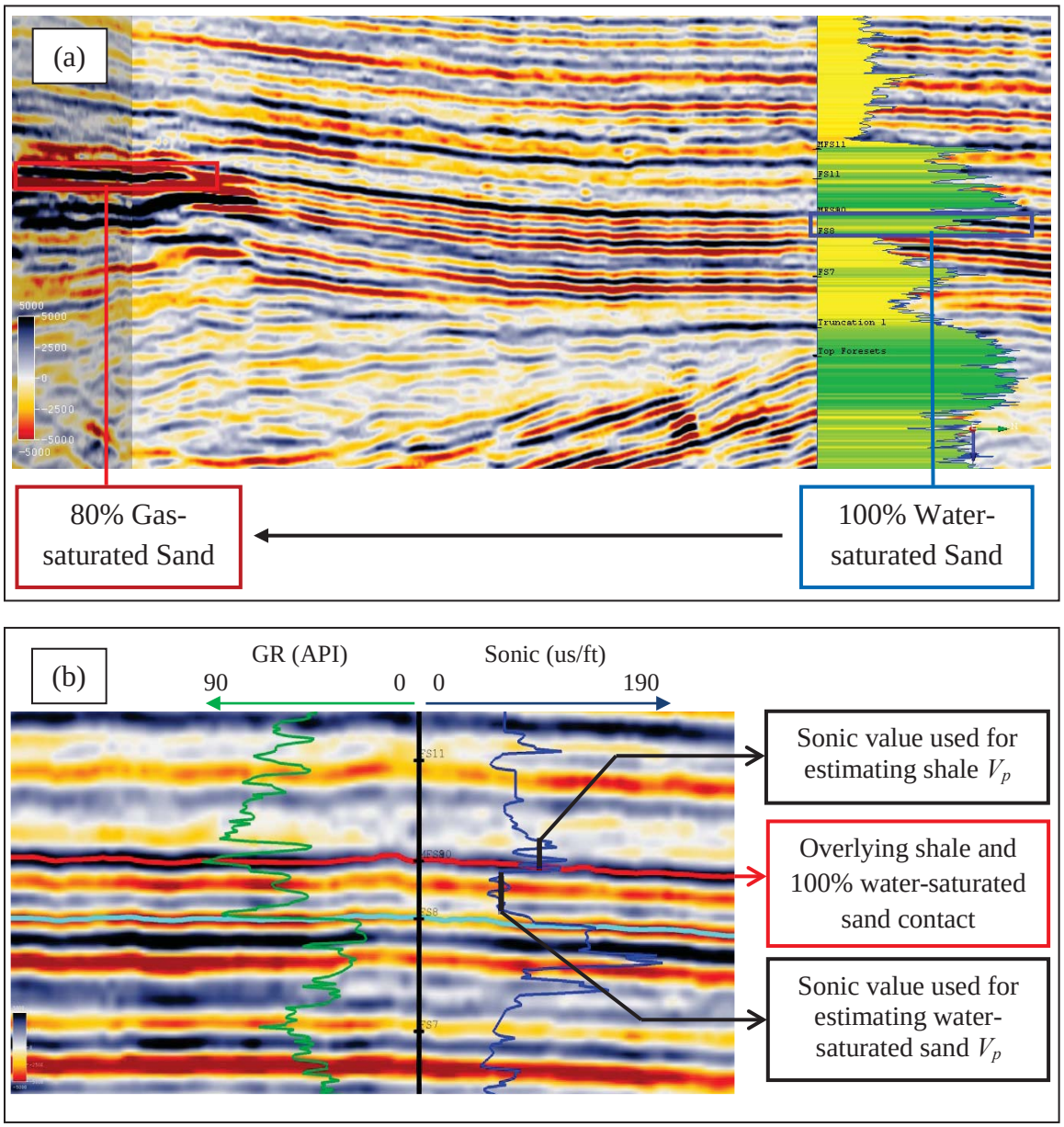

Figure 3.1. (a) Well (F03-4) location and water-saturated sand with respect to the reservoir and picked water-saturated sand layer. The log displayed is Gamma Ray, and the values shown range from 0 near the well-track to 90 API. Colors of the seismic display are those described in Figure 1.1; (b) Well (F03-4) displaying GR and sonic log in detail with respect to water-saturated sand (tracked horizons: red line indicates the top of wet-sand, GWC; green line indicates the bottom of wet-sand), and sonic velocities used for estimating Vp of overlying shale and 100% water-saturated sand. The log displayed is from 500ms to 630ms depth. Colors of the seismic display are those described in Figure 1.1.

Table 3.1. List of all parameters used in rock physics modeling.

Formation Properties (from well-logs)		**Fluid Properties**		**Grain Properties**	
V_{p_sand} (m/s)	2343	K_{water} (GPa)	2.20	K_{grain} (GPa)	37.00
V_{p_shale} (m/s)	2056	ρ_{water} (g/cm^3)	1.10	P_{grain} (g/cm^3)	2.65
ϕ_{sand} (%)	38	K_{gas} (GPa)	0.01		
		ρ_{gas} (g/cm^3)	0.10		

The values provided by the sonic log show that the overlying shale has a lower compressional velocity than the water sand, suggesting that the gas zone should not exhibit a brightspot. (It is important to mention here that the sonic-log values are not necessarily high-quality; we have confidence in our picks, but one could argue with them.)

3.1.2. Rock-Physics Modeling Results

To overcome the limited log data available, we used Gardner's law (Gardner et al., 1974) to estimate density; Greenberg and Castagna's (1992) model for the shear velocities, and Gassmann (1951) for fluid substitution (Appendix D) in the sand, assuming 80% gas saturation, assuming normally pressured gas typical of this depth.

The results from Gassmann fluid substitution are shown in Figure 3.2, we can see that the rock is very sensitive to pore-fluid, and replacement of water with gas decreases the impedance dramatically. The results of this rock-physics modeling are listed in Table 3.2, including those for the sand when 80% saturated by gas.

Having estimated the rock properties, forward modeling studies were conducted to study the possible tuning effects, including the effects of post-critical reflections, and are presented in the following sections.

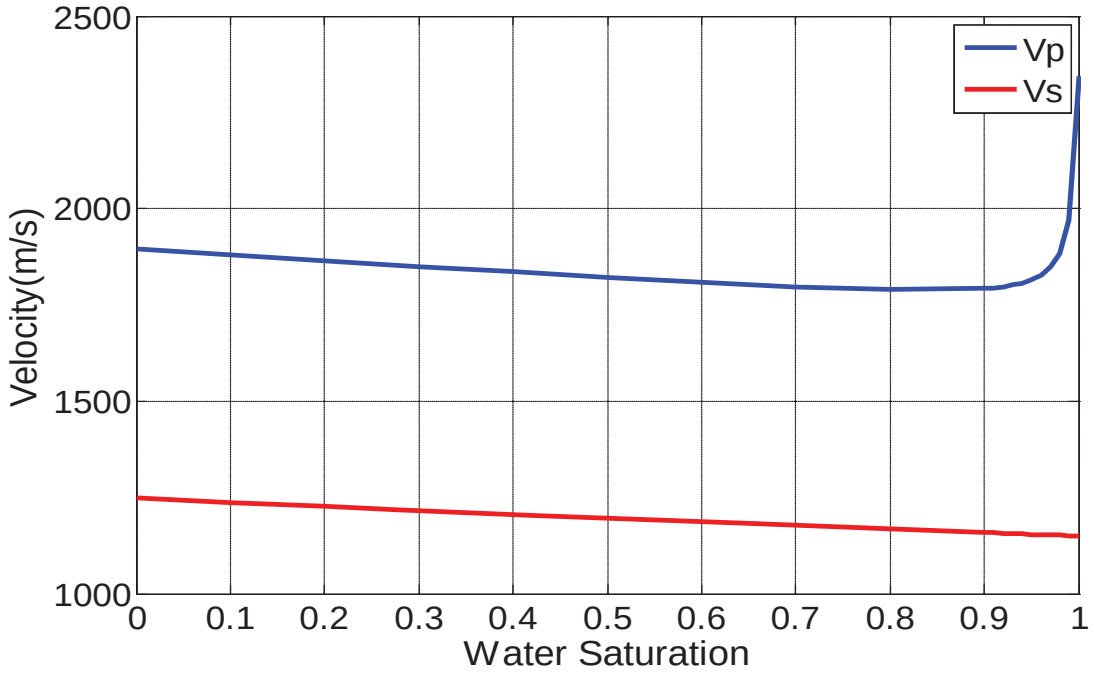

Figure 3.2. Results of substituting water-saturated sand with gas-saturated sand with Gassmann's equation (refer to Appendix D) using parameters in Table 3.1, and Vs of water-saturated sand as estimated by Greenberg and Castagna's (1992) model.

Table 3.2. Results of the rock-physics modeling.

Formation	**Vp (m/s) (from well logs or fluid substitution)**	**Vs (m/s)**	**ρ (g/cm^3) Gardner's law**
Shale	2056	722 (Greenberg & Castagna)	2.08
Gas Sand (Gas saturation = 80%; porosity = 38%))	1850 (Gassmann)	1230	1.90
Water Sand	2343	1150 (Greenberg & Castagna)	2.15

3.2. Tuning Effect Analysis (Zero-Offset)

3.2.1. Synthetic Wedge Model

In order to generalize beyond our specific case, the normal-incidence thin bed tuning effect was analyzed with three different models using only one variable – the acoustic impedance of the overlying shale. By using the observed properties for the water sand and the calculated properties for the gas sand, we varied the properties of the overlying shale to model (1) brightspot over a flatspot, (2) polarity reversal over a flatspot, and (3) dimspot over a flatspot. Details are provided in Table 3.3.

Table 3.3. Hypothetical models (Case 01 and Case 03) for brightspots and dimspots by changing overlying shale properties from the true model (Case 02, polarity reversal).

	Case 01 Brightspot	Case 02 Polarity Reversal	Case 03 Dimspot
Overlying Shale	ρ=2.19 V_p=2380 V_s=966	ρ=2.08 V_p=2056 V_s=722	ρ=1.97 V_p=1710 V_s=450
Gas-Sand	ρ=1.90 V_p=1850 V_s=1230		
Water-Sand	ρ=2.15 V_p=2343 V_s=1150		

A wedge model was used for tuning analysis. A zero-offset synthetic seismic section was generated by convolving a 50 Hz Ricker wavelet (estimated from the spectrum of extracted wavelet from original seismic data) with the geological model. The geological model, the Ricker wavelet and the spectrum of extract wavelet are shown in Figure 3.3. Figures 3.4 show the synthetic seismograms generated for all the three models. The red lines follow the negative (trough) reflections in the region where the tuning effect has distorted the wavelets, while the blue lines show the actual boundary that was present in the wedge model. The green and yellow lines mark the locations where the gas-sand thickness reaches one-fourth of the wavelength (λ/4) and one-eighth of the wavelength (λ/8) respectively.

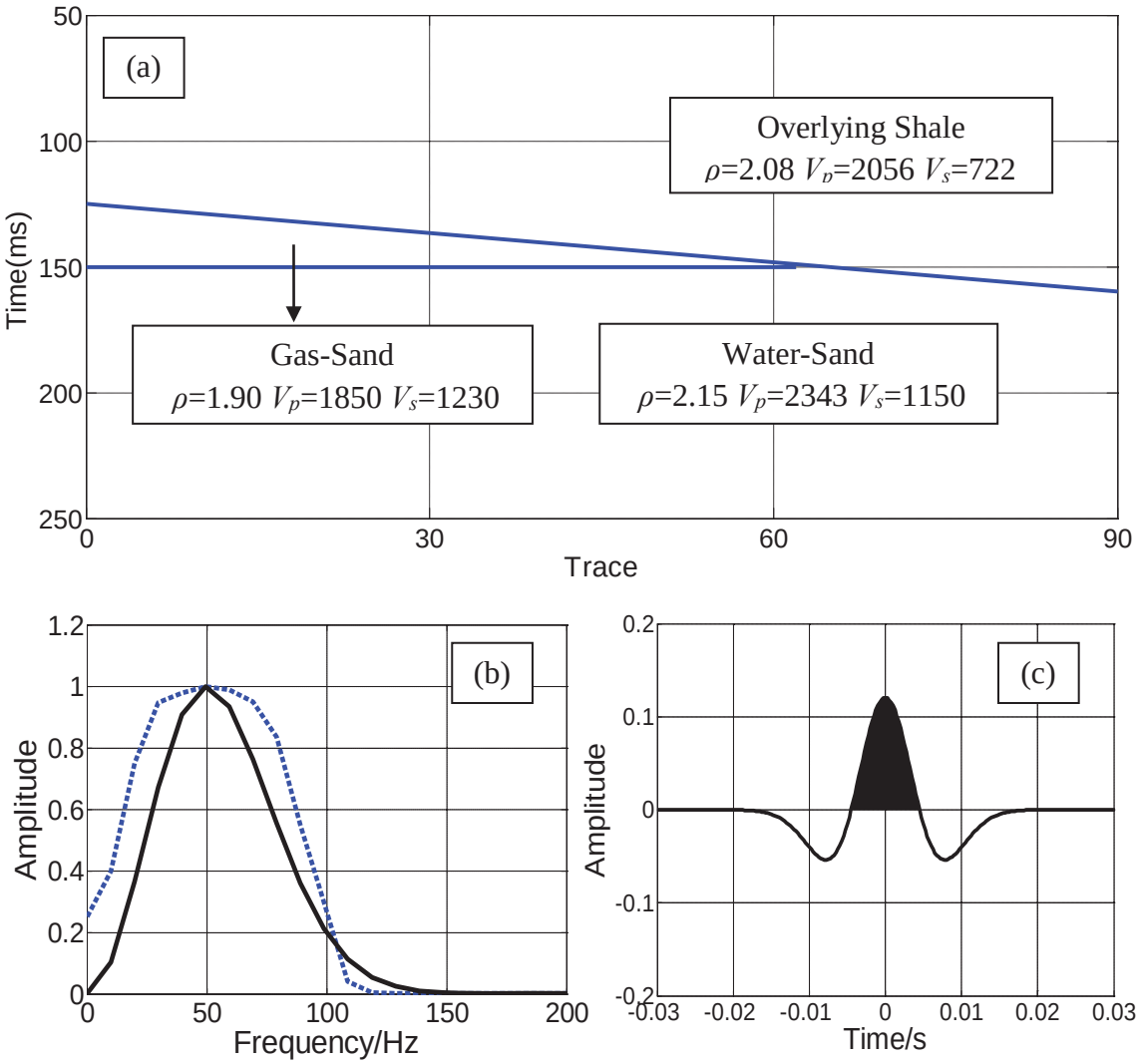

Figure 3.3. The geological model and the wavelet used for modeling. (a) Geological model used for tuning and combination (tuning & stacking) effect analysis and formation properties which are calculated from previous rock physics modeling; (b) Spectrum of extracted wavelet (blue line) from original data and the Ricker wavelet (black line, 50Hz was estimated by picking peak frequency in original wavelet) used for making synthetic seismograms; (c) The 50Hz Ricker wavelet in time domain.

3.2.2. Results from Tuning Effect Modeling

The top model in Figure 3.4 shows the synthetic seismograms for the polarity-reversal (shale impedance is less than that of water sand but greater than that of gas sand); this model best represents the F3 reservoir as estimated from log data. Note that in this model,

the tuning effect near the pinch-out makes the reflection appear nearly flat, changing the dip from 0.36 ms/trace to about 0.15 ms/trace, a reduction by a factor of two, and that at the pinch-out the negative side lobe of the flatspot appears just above the reservoir top.

The synthetic seismograms for the brightspot model (shale impedance is greater than that of both the water sand and the gas sand) are shown in the middle of Figure 3.4. This model shows negligible flattening due to tuning, and interpretation of such a structure is probably straightforward.

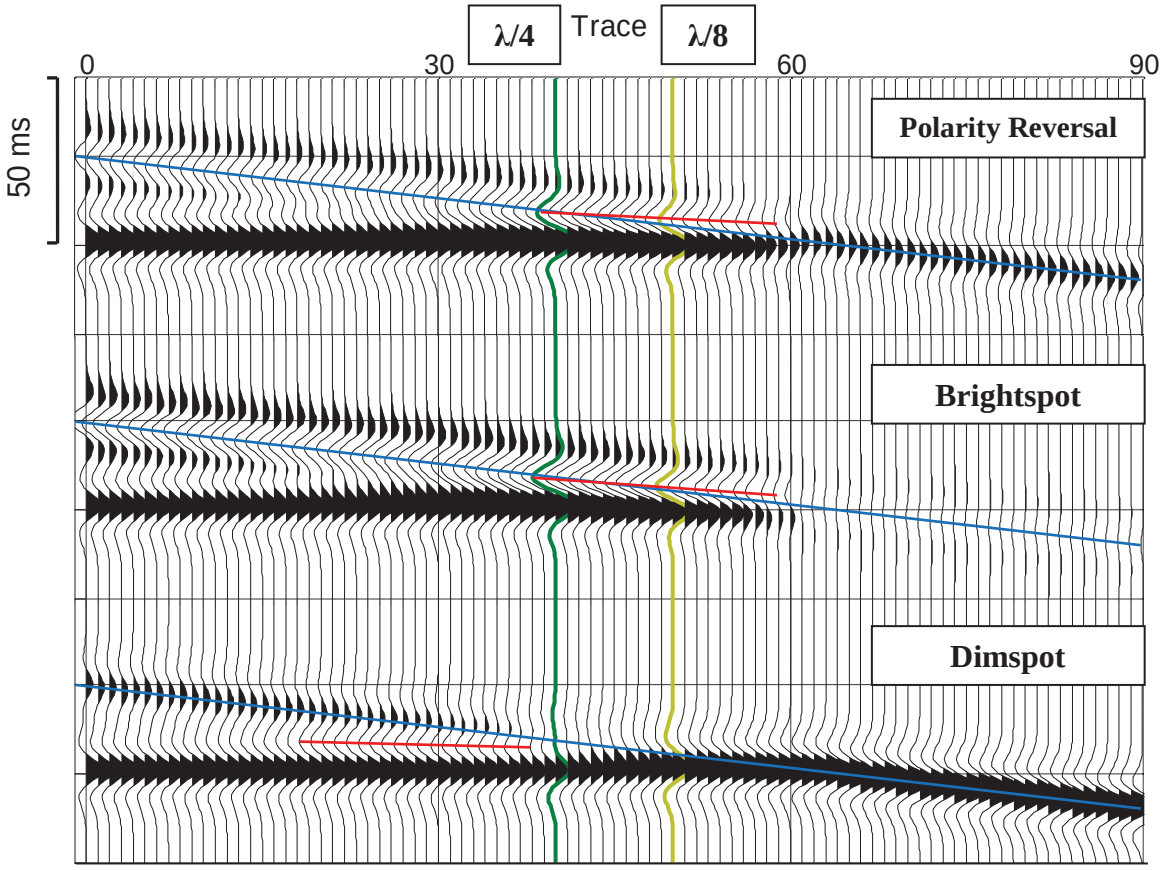

Figure 3.4. Zero-offset seismic section generated by convolving a 50 Hz Ricker wavelet with the wedge model of Figure 3.3a for all the three models and the corresponding comparison of the dip of geological model (blue line) and reflection effected by tuning effect (red line); dip (ms/trace) of blue line **0.36**, and red lines **0.15 (polarity reversal), 0.23 (brightspot), 0.03 (dimspot).**

The results from dimspot modeling are remarkable, as shown in the bottom of Figure 3.4. For a dimspot to occur, the impedance of the shale must be less than that of both the gas sand and the water sand. Because the dimspot is very low-amplitude, the tuning effect at pinch-out is not very important. But the side lobes of the dimspot constructively interfere with the side lobes of the underlying flatspot at thicknesses greater than the tuning thickness (1/4 of the wavelength), eventually weakening as the hydrocarbon zone thickens; it is possible that one's eye, however, would continue to follow the negative side lobe of the flatspot. The resulting seismic section shows a strong negative flat reflection over a strong positive flat reflection; this response is similar to that observed in F3 (Figure 1.1). These reflections exhibit a dip of 0.03 ms/trace rather than the model dip of 0.36 ms/trace.

We have shown that tuning effects can have significant effects on the flatness of bright reflections in the case of a dipping interface with a flatspot terminating against it. In the next section, we analyze and discuss another possible effect: stacking of reflections beyond the critical offset, and combining that with the tuning effects described here.

3.3. AVO & Stacking Beyond Critical Offset

3.3.1. AVO Analysis

Typically, AVO responses are categorized into four classes as defined by Rutherford and Williams (1989) and Castagna (1992). In contrast to these, the negligible shear velocity contrast across any flatspot makes its AVO response distinctive and unique; that is, the reflection coefficient for any flatspot is always positive and always increases with offset, as shown in Figure 2.3.

Figure 3.5 shows the AVO curves (calculated using the full Zoeppritz solution as written by Aki and Richards, 1980, and provided in the Appendix B as Equation B.1) for all four direct hydrocarbon indicators. For reflections that occur at an interface where the velocity increases, a critical angle will be encountered, and beyond that critical angle the reflections will undergo strong phase rotation. Both flatspots and dimspots will always

exhibit supercritical phase rotation (see flatspot and dimspot curves in Figure 3.5b, referring to Equation B.1 and B.2); for flatspots, the critical angle may occur at surprisingly shallow angles, such as the 52° shown in our example. The velocity increase across a flatspot can be significant, particularly for shallow sands, the critical angle is likely to be within the range of recorded data. Because post-critical reflections always undergo phase rotation, if stacking involves these post-critical reflections then the stacked output will exhibit large-amplitude non-zero-phase wavelets. This effect may compound the similar wavelet distortion caused by tuning.

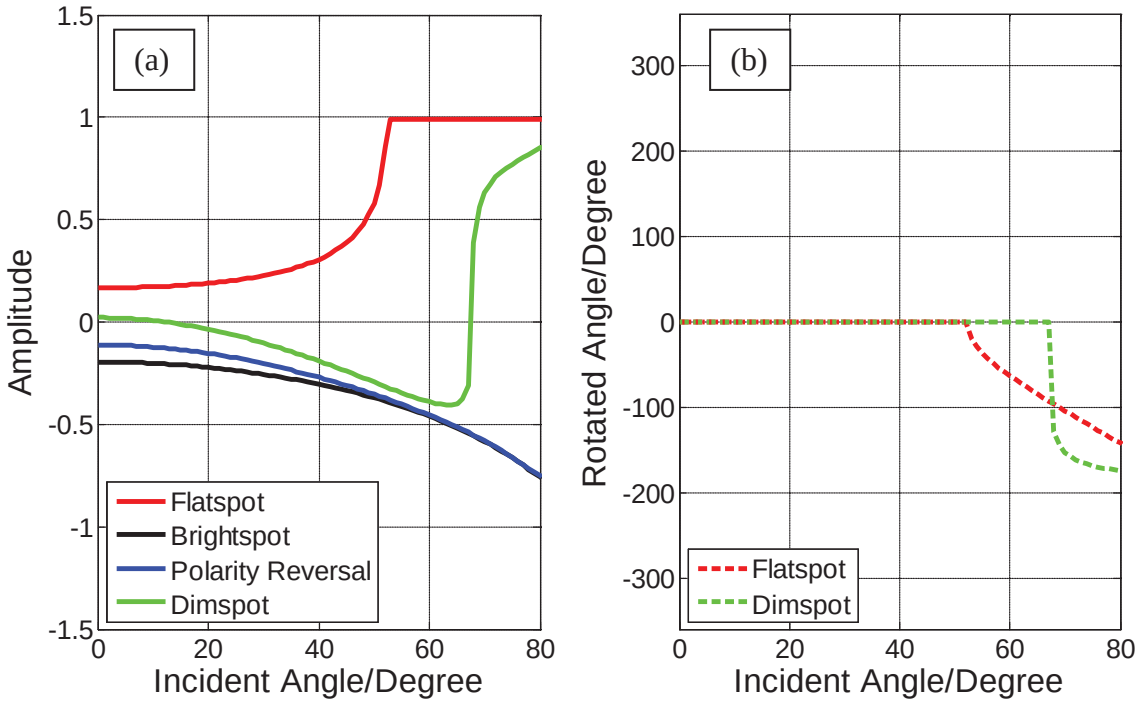

Figure 3.5. (a) AVO responses for three different models (brightspot, polarity reversal & dimspot) and flatspot (GWC); (b) Rotated phase (beyond critical angle) versus incident angle for flatspot and dimspot, noticing these two are the only ones that will show any non-zero phase rotation.

Figure 3.6 shows the result of convolving the AVO response in Figure 3.5 (including phase shifts for the flatspot and dimspot that extend beyond critical) with a 50Hz Ricker wavelet. The far-right seismograms show the result of stacking these over different angle ranges.

As the stacking ranges increase, all hydrocarbon indicators other than the flatspot show an increase in brightness without any change in wave shape (the dimspot model does not include many traces beyond critical, and the effect of its phase rotation is minimal in this model). The flatspot on the other hand shows not only an increase in amplitude but also a change in shape. For example, a zero phase Ricker wavelet when stacked over a range of 0 to 70 degrees approaches a 90° wavelet; the earliest part of this is a "trough" which in turn appears as if it could have been caused by a negative reflection coefficient at zero-offset. Hence, flatspot events stacked beyond critical offset can generate spurious bright reflections that might be categorized as 'brightspots' by the interpreters. Muting based only on the NMO stretch may not remove the post-critical reflections and could mislead the interpreters. Because muting is usually based on distortion caused by NMO, and not by angle, it is possible that some flatspots are stacked beyond critical angle.

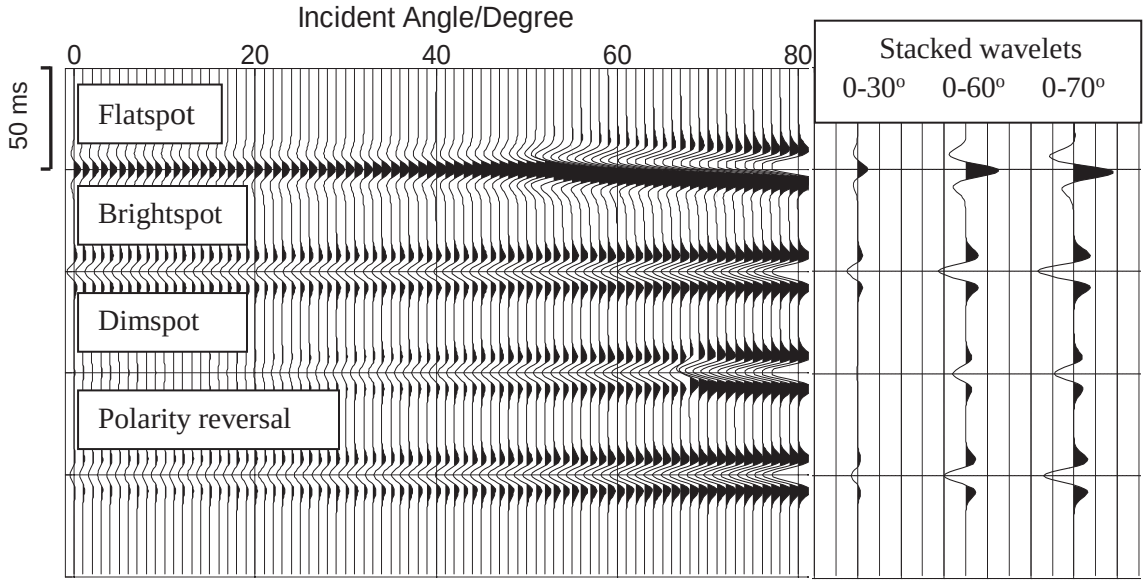

Figure 3.6. Seismic AVO responses for different models, using a 50Hz Ricker wavelet. The figure at the right shows the stacked wavelet when stacked over different angle ranges.

3.3.2. Synthetic Stacked Seismograms (Combined Effect of Tuning & Stacking)

As we have seen, a zero-phase Ricker wavelet, when stacked over a range of 0° to 70°, undergoes a significant phase rotation and, in the presence of noise, might appears as a

negative reflection event. Hence, flatspot events stacked beyond critical offset can generate reflections that might be categorized as ‘brightspot’ by the interpreters.

To see the combined effect from tuning (due to dipping interface encountering a flatspot) and post-critical reflections (which undergo phase shifts), we ran the wedge model described earlier, but this time used wide-angle stacks rather than zero-offset reflections. Three different models (polarity reversal, brightspot and dimspot) were prepared for 0-30^0, 0-60^0 and 0-70^0 stacks, respectively, recalling that the critical angle for the flatspot in this model is 52^0. The synthetic seismograms shown in Figures 3.7-3.9 show that the combined effect of tuning and supercritical stacking enhances the flatness of those spurious bright reflections. Table 3.4 summaries the dip in ms/trace of reflections affected by tuning effects and stacking ranges compared with original geological model dip, for three different models.

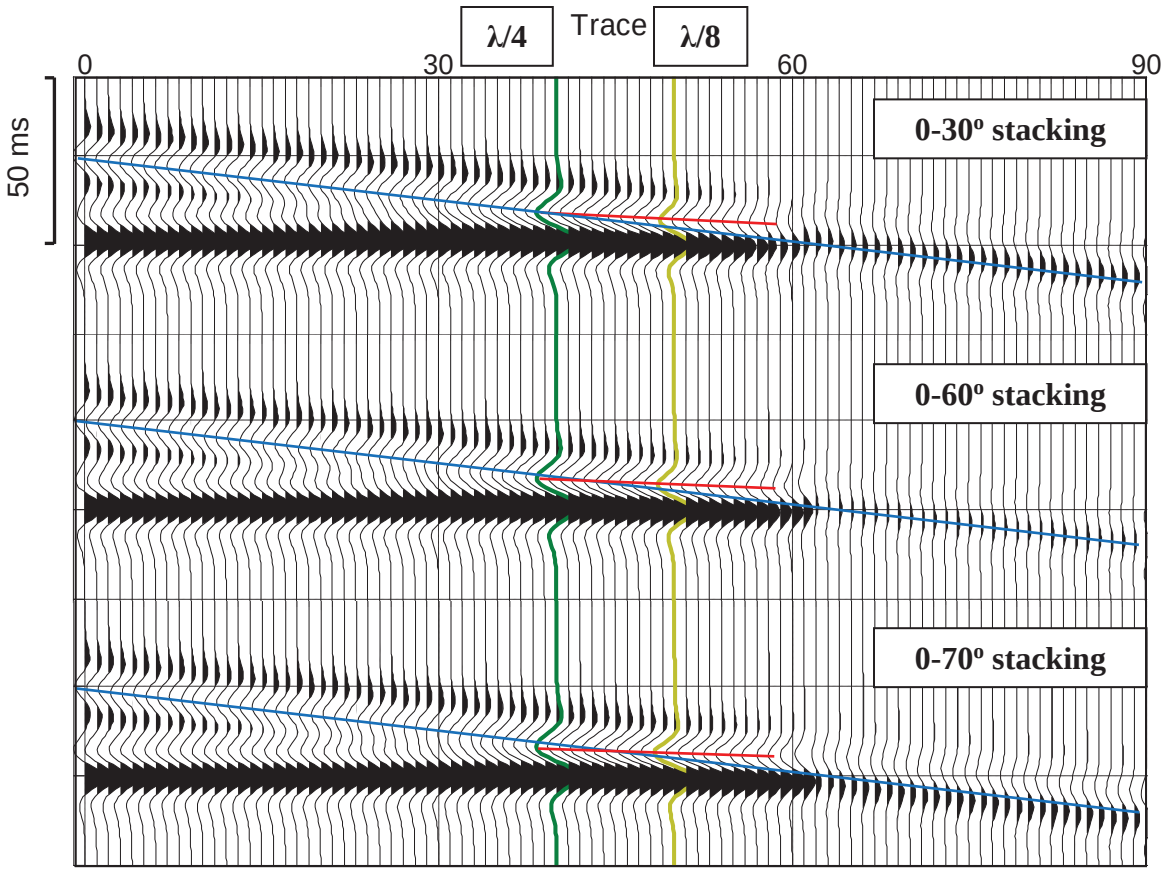

Figure 3.7. Modeled seismogram displaying the combined effect of thin-bed tuning & different angle ranges of 0-30º, 0-60º and 0-70º stacking for the **polarity reversal** case and the corresponding comparison of the dip of geological model (blue line) and reflection effected by tuning effect & stacking (red line); dip (ms/trace) of blue line **0.36**, and red lines **0.15 (0-30º stacking), 0.13 (0-60º stacking), 0.10 (0-70º stacking).**

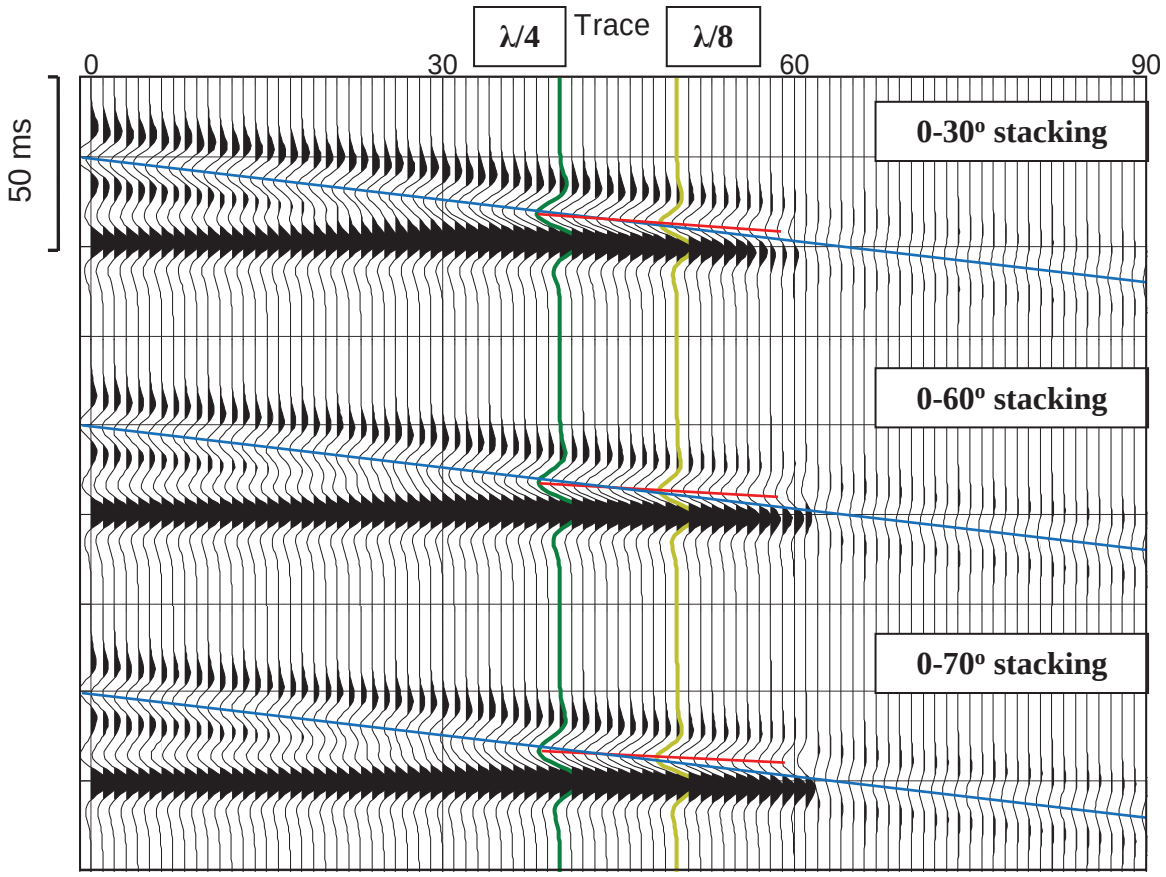

Figure 3.8. Modeled seismogram displaying the combined effect of thin-bed tuning & different angle ranges of 0-30^{o}, 0-60^{o} and 0-70^{o} stacking for the **brightspot** case and the corresponding comparison of the dip of geological model (blue line) and reflection effected by tuning effect & stacking (red line); dip (ms/trace) of blue line **0.36**, and red lines **0.23 (0-30º stacking), 0.18 (0-60º stacking), 0.15 (0-70º stacking).**

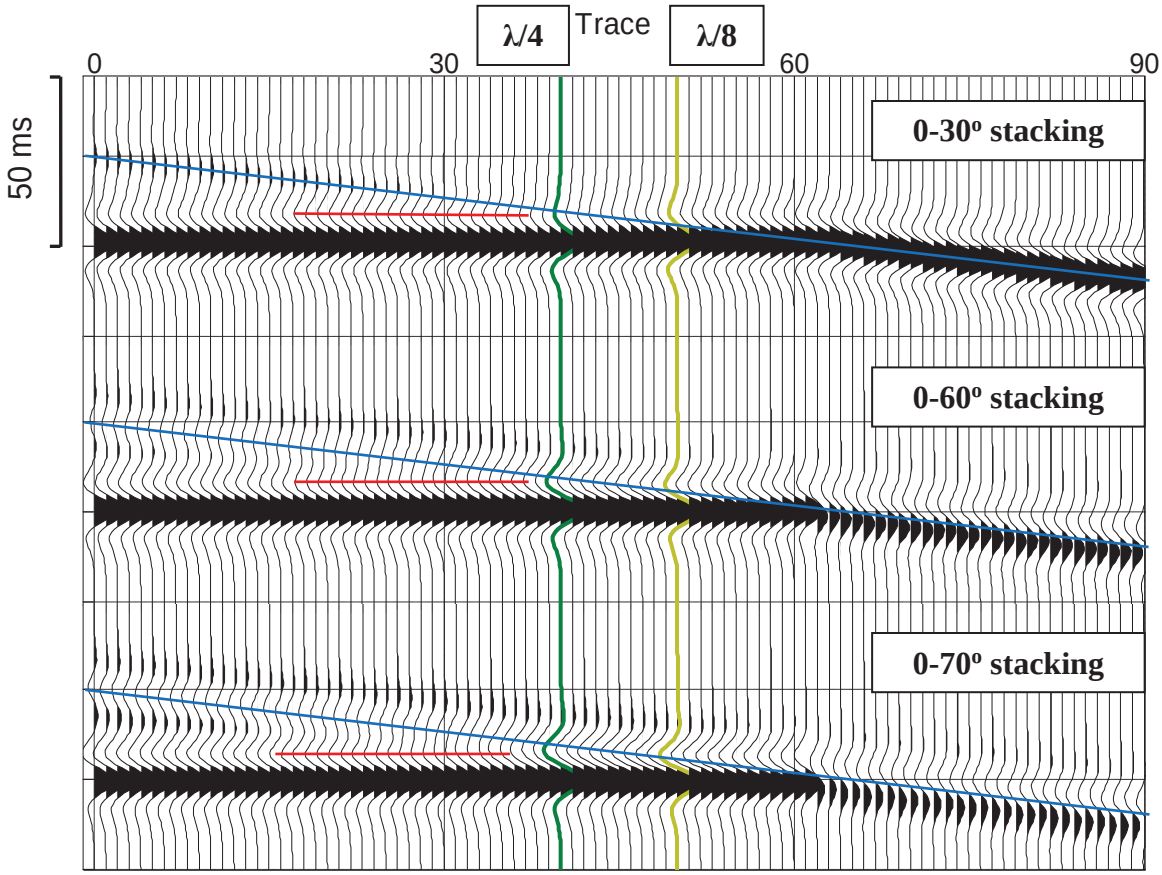

Figure 3.9. Modeled seismogram displaying the combined effect of thin-bed tuning & different angle ranges of 0-30º, 0-60º and 0-70º stacking for the **dimspot** case and the corresponding comparison of the dip of geological model (blue line) and reflection effected by tuning effect & stacking (red line); dip (ms/trace) of blue line **0.36**, and red lines **0.03 (0-30º stacking), 0.00 (0-60º stacking), 0.00 (0-70º stacking).**

The modeling results summarized in Table 3.4 show a significant decrease in dip angle for all models. This suggests that observed reflection events from the top of the reservoir can appear as a "flat" event, discordant to the structural trend, because of tuning. The effect is most striking if the top of the reservoir exhibits a polarity reversal over the gas zone. Even the brightspot model shows that stacking beyond critical, combined with tuning, can result in some apparently flatter events, although the larger (brighter) reflection from the reservoir top probably helps avoid improper interpretation. But the maximum flattening effect was observed from the dimspot model. These flat reflections

were caused by the tuning effect and are exaggerated when the non-zero-phase wavelet is stacked in beyond critical. The sonic log from a nearby well suggests that the reservoirs in the F3 Block most likely exhibit a polarity reversal, but the dimspot model seems to best match the F3 seismic data, based on visual examination of multiple shallow gas zones.

Table 3.4. Summary and comparison of the dip (ms/trace) of the geological structure and for the reflections from three different models with stacking over different angle ranges.

Dip/Flatness (ms/trace)		**Model types**		
		Polarity reversal	**Brightspot**	**Dimspot**
Geological model (Structural trend)		*0.36*	*0.36*	*0.36*
Stacking range	**Zero-offset (Tuning effect only)**	*0.15*	*0.23*	*0.03*
	Stacking over 0-30°	*0.15*	*0.23*	*0.03*
	Stacking over 0-60°	*0.13*	*0.18*	*0.00*
	Stacking over 0-70°	*0.10*	*0.15*	*0.00*

For our particular dataset, we do not know what muting criterion had been used in the original processing nor how much stretch was caused by NMO correction to either pre-critical or post-critical reflections, so the previous discussion and analysis were restricted to stretch-free modeling. In the next section, NMO stretch and muting will be considered in our analysis.

3.4. NMO Stretch and Muting Analysis

3.4.1. Subsurface Model

In order to estimate possible NMO stretch for different mutes, based on established industry standards, we expanded our modeling to include these effects, in order to examine the effects that NMO stretch might have.

Based on the well log data (gamma ray and sonic logs), we created a simple subsurface model with homogenous flat layers above the gas reservoir (Figure 3.10). Within the vicinity of the gas reservoir, we used parameters obtained earlier for the polarity-reversal case only. The model is intended to resemble the area of block F3, and we obtained depths to the different layers by converting seismic travel times through appropriate interval velocities in order to ensure that the one thick overlying layer would scale properly. In this model, the offset to the critical angle (the "critical offset") for the flatspot reflection is approximately 1300m.

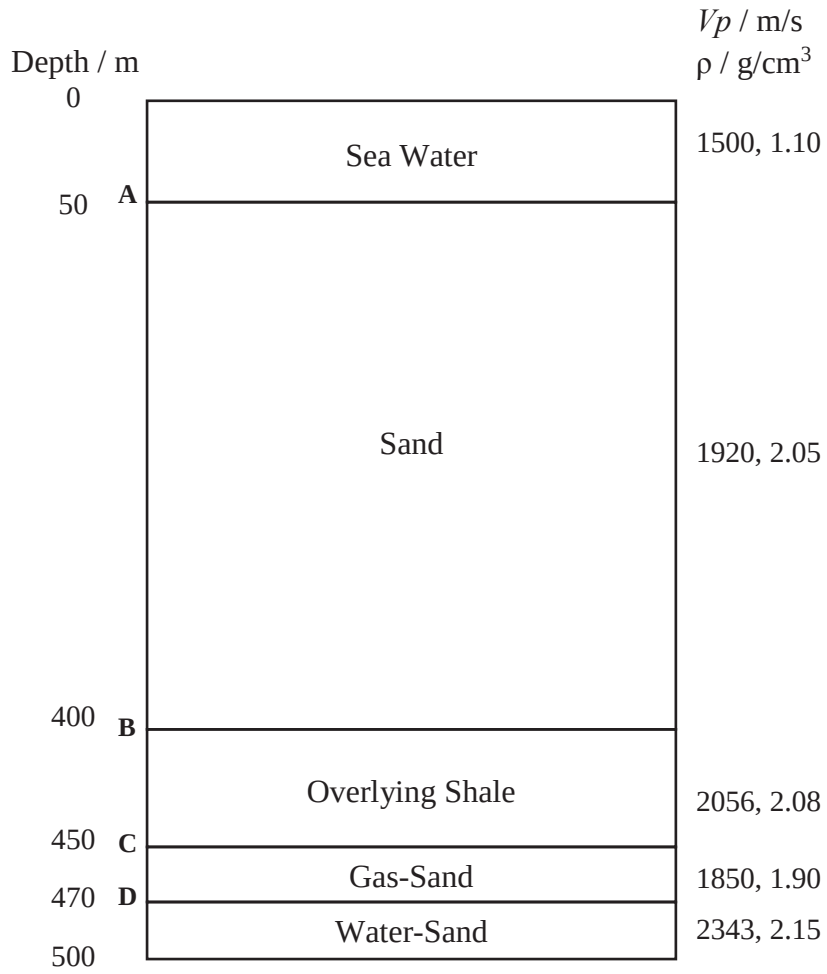

Figure 3.10. The assumption of subsurface model (homogenous flat layers) and the estimated parameters associated with them above gas reservoir in F3 Block (A, B, C and D represent corresponding reflections in Figure 3.11a).

3.4.2. NMO Stretch and Muting Analysis

Based on the 'percent of changing frequency' criterion (Yilmaz, 1987), our model suggests that reflections from gas/water contact could be automatically muted. This criterion yields muting at 1100m offset for the time of the flatspot reflection, and the critical angle is encountered at around 1300m offset. The details are provided in Figure 3.11, which show the synthetic CMP gather before NMO correction, after NMO correction without muting and after muting. Notice the seismic data beyond critical offset (X=1300m) for the flatspot reflection has been muted.

In addition, the reflection hyperbolae intersection of the seafloor reflection with the flatspot reflection can be observed at around 1200m. Because the maximum NMO stretch usually occurs when some of the reflection hyperbolae intersect one another (Buchholtz, 1971; Andrew et al., 1999; Zhang et al., 2011), the traces around that offset are often muted; in our case, this offset happens to be close to the critical offset for the flatspot reflections. We conclude that the post-critical seismic data from flatspot reflections in F3 were most likely muted during pre-stacking and excluded from the stacked output.

3.4.3. Results and Comparison with Original Seismic Data

Based on the analyses described above, reflections from gas/water contact are likely to have been muted beyond 1100 m offset, corresponding to an angle of incidence of 47°. Figure 3.12a shows the synthetic seismograms that result from stacking over angle range of 0-47° for the polarity reversal case previously shown for different angle ranges. This perhaps best represents the case in the dataset we studied in North Sea Block F3. The synthetic seismograms demonstrate the flat, bright reflections caused by tuning and stacking. We think that this explains the observations in the seismic data, as shown in Figure 3.12b.

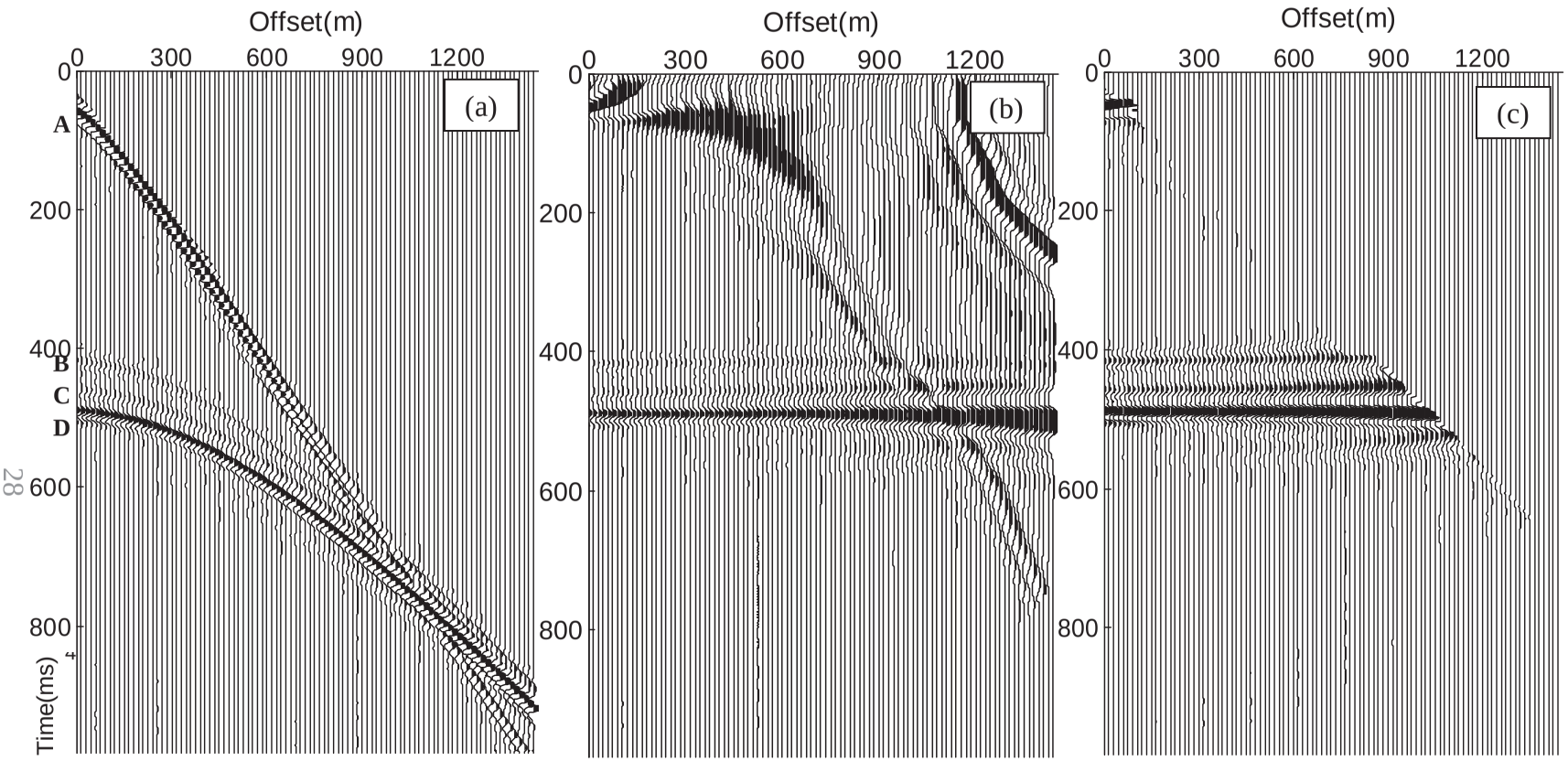

Figure 3.11. NMO stretch and muting analysis on the CMP gather associated with subsurface model. (a) Synthetic seismogram of CMP gather associated with subsurface model before NMO correction (A: sea water/sand; B: sand/overlying shale; C: overlying shale/gas-sand; D: gas-sand/water-sand), notice the intersections of reflection hyperbolae A with B, C and D at far offset (X=1200 m); (b) Synthetic seismogram of CMP gather associated with subsurface model after conventional NMO correction without muting, notice the distortion of wavelets caused by the NMO stretch (especially for shallow and far-offset reflections); (c) Synthetic seismogram of CMP gather associated with subsurface model after traditional NMO correction and muting, notice seismic data beyond the critical offset (X=1300 m) for flat reflection has been muted.

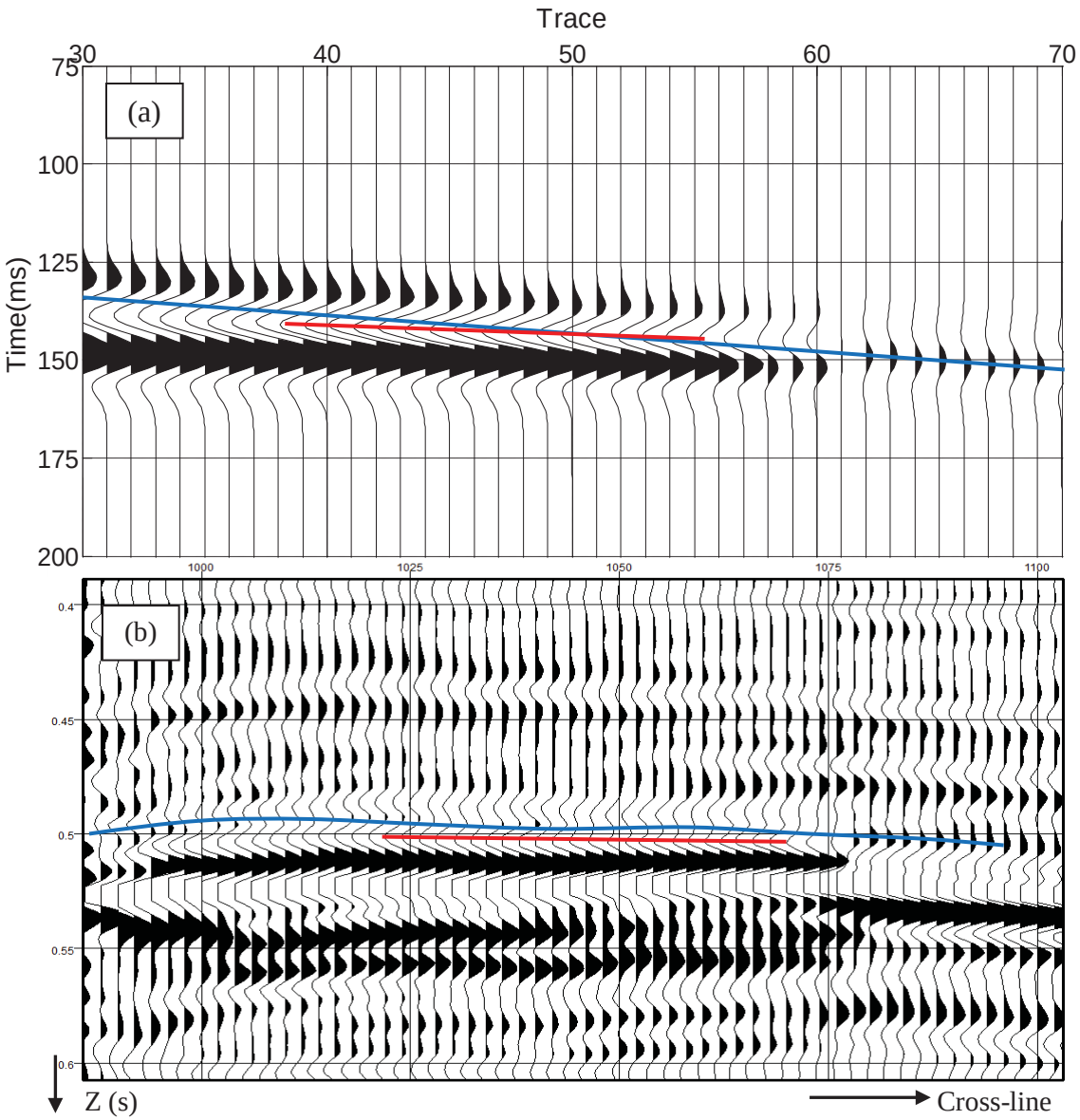

Figure 3.12. The comparison between stacking synthetic seismogram and original seismic data. (a) Synthetic of stacking seismogram with angle range of 0-47º for the polarity reversal case representing the post-stacked seismic with NMO muting; (b) Original post-stacked seismic data in North Sea F3 Block provided by the OpendTect. Blue line indicates dip of geological model in Figure 3.12a and the true structural trend in Figure 3.12b (based on a phantom horizon); red lines indicate the flatness of a bright reflection.

4. Results and Discussion

Bright reflections in the F3 Block of the North Sea were analyzed for possible sources of their flatness. Tuning effects and post-critical stacking were evaluated as possible reasons. For this purpose, zero-offset and wide-angle stacked sections were prepared by forward modeling, and NMO stretch and muting were investigated in order to evaluate the possibility that stacking extended beyond the critical offset for our dataset.

The tuning effect results showed significantly decreasing reflection dip for polarity reversal and dimspot cases: for polarity reversal (the geological model based on well logs), the synthetic seismograms show that the reflections become very flat due to a tuning effect for thicknesses under 1/4 wavelength. For the dimspot case, the modeling results are even more remarkable: because the dimspot event is very low-amplitude, the tuning effect caused by the underlying flat reflection is very important. As the dimspot side lobes constructively interfere with the flatspot side lobes at thicknesses greater than the tuning thickness, and as they destructively interfere (dim reflections are buried in bright reflections) at thicknesses smaller than the tuning thickness, the trend of the dimspot reflection is dominated by the flatness of the flatspot reflection. The result for the dimspot is a strong negative flat reflection over a strong positive flat reflection; this response is similar to that observed in F3.

If post-critical events were included in the stacking output for our data set, additional distortion to the event could have resulted, so we studied the AVO response together with wide-angle stacking. Flatspot events stacked beyond critical offset can generate spurious bright reflections that might be categorized as ‘brightspots’, and the two phenomena (tuning effect and supercritical stacking) could act together largely modifying the final results in actual reservoir. This effect is even more striking if the top of the reservoir exhibits a polarity reversal over the gas zone. For our particular dataset, the stretching and muting is unknown, but our simple models suggest that post-critical seismic data was excluded in stacking output.

Based on these analyses, it can be concluded that both tuning effects and post-critical stacking can make bright reflections in F3 flatter and brighter, but that post-critical stacking likely did not occur, and the tuning effect is presumed to be the main source of the bright, flat events in the F3 data. The tuning effects can be significant for both dimspots or polarity reversals, making these reflections appear as ‘brightspots’. Care should always be used when interpreting stacked data, with the recognition that it is not the same as zero-offset data.

5. Conclusion

The stacking of flatspot reflections beyond critical angle can boost their amplitude significantly while accompanied by a significant phase shift in the stacked output. Thin-bed effects can also result in tuning that can change amplitudes and apparent polarity and phase in cases we examined. Individually, these effects can result in fairly flat, bright negative events overlying strong positive reflections. The effect can be strong enough that it can even make a dimspot appear as a (flat) bright spot.

The NMO stretch and muting analysis shows that post-critical seismic data of flat reflections was most likely excluded in the stacking output from our dataset. We conclude that the tuning effect is the key reason for the flatness of the bright-reflections at shallow depths of the North Sea. We further conclude that these bright reflections are not typical ‘brightspots’ but appear as such because of the tuning effect.

In addition, although for our particular dataset, post-critical offset data were probably muted based on traditional criteria, we recommend that care should be taken while dealing with reflection data containing wide range of incidence angles where those criteria may not be routinely applied (e.g., cross-well seismic data). In addition, muting applied solely on the basis of NMO stretch might include post-critical reflections and the stacked output will be significantly altered.

References

Aki, K., and P. G. Richards, 1980, Quantitative seismology-Theory and Methods, 1: *W.H. Freeman and Co.*

Buchholtz, H., 1972, A note on signal distortion due to dynamic (NMO) corrections: *Geophysics Prospecting*, **20**, 395-402.

Brown, A. R., 2010, Dim Spots in Seismic Images as Hydrocarbon Indicators: Search and Discovery Article, *American Association of Petroleum Geologists*.

Brown, A. R., 2012, Dim spots: Opportunity for future hydrocarbon discoveries: *The Leading Edge*, **31**, 682-683.

Bortfeld, R., 1961, Approximation to the reflection and transmission coefficients of plane longitudinal and transverse waves: *Geophysical Prospecting*, **9**, 485-503.

Castle, R. J., 1994, A theory of normal moveout: *Geophysics*, **59**, 983-999.

Castagna, J. P., H. W. Swan, and D. J. Foster, 1998, Framework for AVO gradient and intercept interpretation: *Geophysics*, **63**, 948-956.

Chopra, S., J. Castagna, and O. Portniaguine, 2006, Seismic resolution and thin-bed reflectivity inversion: *CSEG Recorder*, **31**, no. 1, 19-25.

Dix, C. H., 1955, Seismic velocities from surface measurements: *Geophysics*, **20**, 68-86.

Dunkin, J. W., and F. K. Levin, 1973, Effect of normal moveout on a seismic pulse: *Geophysics*, **38**, 635-642.

Forrest, M., 2000, Bright ideas still needed persistence: *AAPG Explorer*, **21**, no. 5, 20-21.
Gardner, G. H. F., L. W. Gardner, and A. R. Gregory, 1974, Formation velocity and density-the diagnostic basics for stratigraphic traps: *Geophysics*, **39**, 770-780.

Gassman, F., 1951, Uber die elastizitat poroser medien: *Vierteljahrschrift Der Naturforschenden Gesellschaft in Zurich*, **96**, 1-21.

Greenberg, M. L., and J. P. Castagna, 1992, Shear-wave velocity estimation in porous rocks: theoretical formulation,bpreliminary verification and applications: *Geophysical Prospecting*, **40**, 195-210.

Hilterman, F. J., 2001, Seismic amplitude interpretation-distinguished instructor short course: *Society of Exploration Geophysicists and European Association of Geoscientists and Engineers*.

Kallweit, R. S., and L. C. Wood, 1982, The limits of resolution of zero-phase wavelets: *Geophysics*, **47**, 1035-1046.

Knott, C. G., 1899, Reflection and refraction of elastic waves with seismological applications: *Phil. Mag*., **48**, 64-97.

Koefoed, O., 1955, On the effect of Poisson's ratios of rock strata on the reflection coefficients of plane waves: *Geophysical Prospecting*, **3**, 381-387.

Ostrander, W. J., 1984, Plane wave reflection coefficients for gas sands at non-normal angles of incidence: *Geophysics*, **49**, 1637-1648.

Robertson, J. D., and H. H. Nogami, 1984, Complex seismic trace analysis of thin beds: *Geophysics*, **49**, 344–352.

Rupert, G. B., and J. H. Chun, 1975, The block move sum normal moveout correction: *Geophysics*, **40**, 17-24.

Rutherford, S. R., and R. H. Williams, 1989, Amplitude-versus-offset variations in gas sands: *Geophysics*, **54**, 680-688.

Ricker, N., 1953, Wavelet contraction, wavelet expansion and the control of seismic resolution*: Geophysics*, **18**, 769-792.

Schroot, B. M., and R. T. E. Schuttenhelm., 2003, Expressions of shallow gas in the Netherlands North Sea: *Netherlands Journal of Geosciences*, **82**(1): 91-106.

Shatilo, A., and F. Aminzadeh, 2000, Constant normal-moveout (CNMO) correction: a technique and test results: *Geophysical Prospecting*, **48**, 473-488.

Shuey, R. T., 1985, A simplification of the Zoeppritz equations: *Geophysics*, **50**, 609-614.

Widess, M. B., 1973, How thin is a thin bed?: *Geophysics*, **38**, 1176-1180.

Yilmaz, O., 1987, Seismic Data Processing (Investigations in Geophysics, Vol. 2): *Society of Exploration Geophysicists.*

Zhang, B., K. Zhang, S., Guo and K. J. Marfurt, 2013, Nonstretching NMO correction of prestack time-migrated gathers using a matching-pursuit algorithm: *Geophysics*, **78**, U9-U18.

Zoeppritz, K., 1919, Erdbebenwellen VIIIB, On the reflection and propagation of seismic waves: *Gottinger Nachrichten*, **I**, 66-84.

Appendix A: Direct Hydrocarbon Indicators

The use of direct hydrocarbon indicators (DHIs) including brightspots, dimspots, and flatspots, has frequently assisted in the success of exploration projects, since the widespread application of brightspot technology in the oil industry starting in the late 1960s (Forrest, 2000).

A conventional hydrocarbon reservoir is made up of porous and permeable rock that contains hydrocarbons which lower the acoustic impedance in contrast to similar rock saturated entirely with water. If the reservoir rock is overlain by a higher-impedance formation, there will be larger negative acoustic impedance contrast between the reservoir and surrounding water-saturated rock, resulting in a high amplitude (negative) seismic reflection, called a brightspot. By definition, a brightspot is always characterized by a strong negative reflection coefficient over the reservoir with a weaker negative reflection event on the sides or edges (Figure A.1).

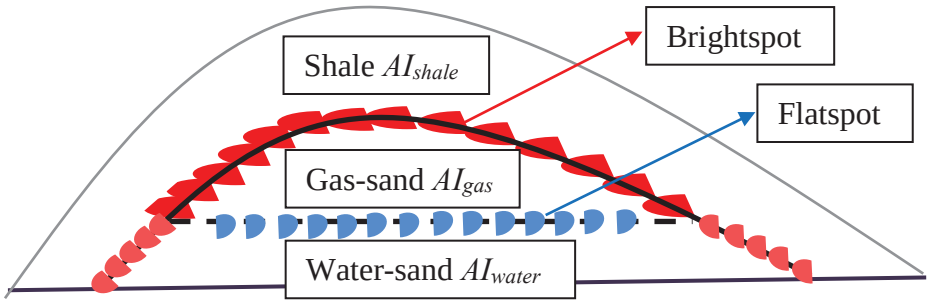

Figure A.1. Schematic diagrams for **brightspot** ($AI_{shale} > AI_{water} > AI_{gas}$), AI_{shale} AI_{water} and AI_{gas} represents acoustic impedance of shale, water sand and gas sand respectively. Red indicates a decrease in impedance; blue an increase.

If instead of being overlain by a higher-impedance formation, the reservoir rock is overlain by a lower-impedance formation, then the replacement of water with hydrocarbons will cause a decrease in impedance contrast between the reservoir and surrounding rock frame. The end result is a weaker positive reflection over the reservoir contrasted with a stronger positive reflection at the water-saturated rock at and beyond the reservoir edges (Figure A.2). This is called a dimspot. In some cases, the impedance

of the overlying formation is only slightly higher than that of the hydrocarbon-saturated reservoir rock, and slightly lower than similar rock saturated with water; in that case, there will be a polarity reversal from a weak negative over the reservoir to weak positive reflections at the edges (Figure A.3). Dimspots are difficult to identify, and one can easily miss them because of their negligible amplitudes and the tendency to track an associated flatspot instead (both are positive reflections). But brightspots and dimspots equally suggest the presence of hydrocarbons, and both are equally abundant (Brown 2012).

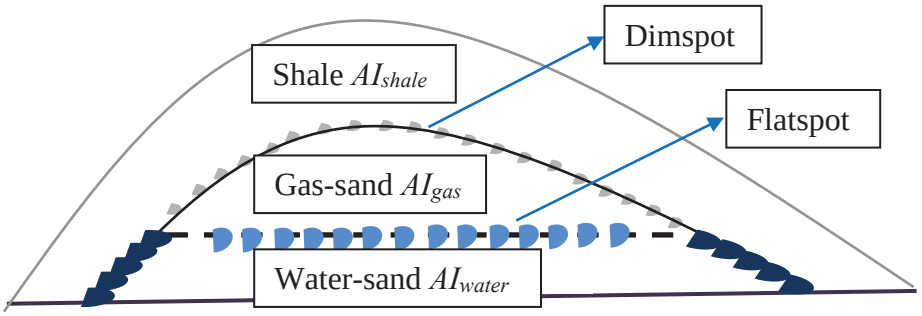

Figure A.2. Schematic diagrams for **dimspot** ($AI_{water} > AI_{gas} > AI_{shale}$), AI_{shale} AI_{water} and AI_{gas} represents acoustic impedance of shale, water sand and gas sand respectively. Red indicates a decrease in impedance; blue an increase.

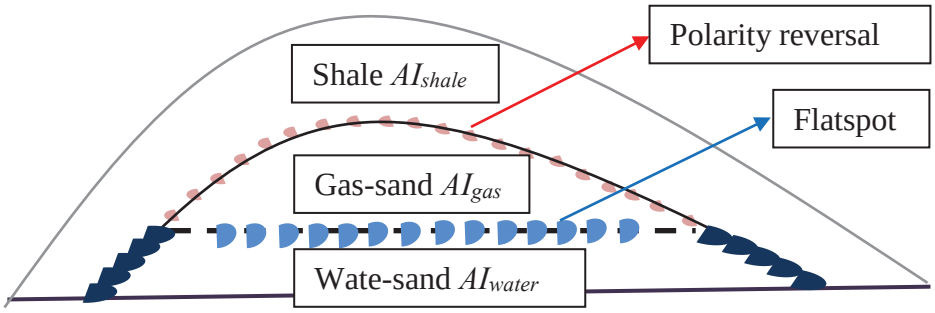

Figure A.3. Schematic diagrams for **polarity reversal** ($AI_{water} > AI_{shale} > AI_{gas}$), AI_{shale} AI_{water} and AI_{gas} represents acoustic impedance of shale, water sand and gas sand respectively. Red indicates a decrease in impedance; blue an increase.

In contrast to brightspots and dimspots, flatspots indicate the oil-water or gas-water contact within the reservoir. In this case the acoustic impedance difference between two zones is caused only by pore fluid (and water bearing zone has higher AI than hydrocarbon bearing zone) as the rock matrix is supposed to be the same. A flatspot is always characterized by positive reflections that are perfectly flat in contrast to a dipping structural trend of the rock frame.

Because the compaction for sands and shales occurs at different rates and the acoustic impedance relationship between them will change due to different depth or age. Dimspots are expected in deeper horizons where the sand has higher impedance than that of shale. For shallow depths, sand has lower impedance than that of shale, so there are good chances of brightspots (Brown, 2010).

Appendix B: Amplitude Variation with Offset (AVO)

B.1. Non-normal Incident Wave

When a compressional plane-wave impinges upon a plane interface between two semi-infinite homogeneous media with a non-normal incident angle, the wave-energy is split into a maximum of four different components: (1) Reflected P-wave, (2) Transmitted P-wave, (3) Reflected S-wave and (4) Transmitted S-wave (Figure B.1). Snell's law governs the reflection and transmission angle of each wave according to the respective wave velocities in corresponding media. The P-wave reflection coefficient $R_p\ (\theta)$ is defined as the ratio of the reflected P-wave energy to the incident P-wave energy, and is a function of incidence angle and impedance (acoustic & shear) contrast at the interface. The change in reflection coefficient with a change in incidence angle is the fundamental basis for amplitude versus offset (AVO) analysis.

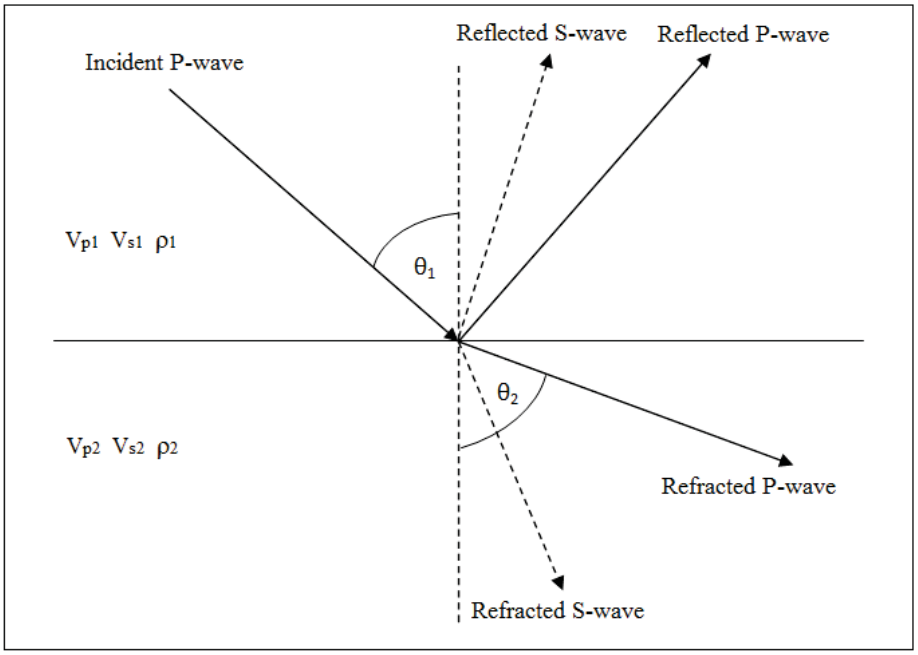

Figure B.1. An incident P-wave reflected off an interface between two medium. Model conversions occur resulting in reflected P- and S- waves and transmitted (refracted) P- and S- waves. θ_1 and θ_2 denote incident angle and refracted angle for P-wave respectively.

B.2. Mathematical Expressions of AVO

Knott (1899) and Zoeppritz (1919), for the first time, developed the theoretical work and gave mathematical expressions of the reflection and transmission coefficients as a function of incidence angle and elastic properties (density, V_p and V_s). However, the exact mathematical equations are very complex and difficult to understand how reflection amplitude varies with changing pore properties (Hilterman, 2001). The equations are modified and approximations to the equations are given by many others e.g., (Koefoed, 1955; Bortfeld, 1961; Aki and Richards, 1980 and Shuey, 1985 etc.).

The following gives the Aki & Richards approximation (1980) of AVO responses for PP reflection coefficients (downgoing P-wave scattered as upgoing P-wave) across a solid-solid interface case (Equation B.1). And this is the formula used for AVO modeling later.

$$R_{pp} = \left[\left(b \frac{\cos i_1}{\alpha_1} - c \frac{\cos i_2}{\alpha_2} \right) F - \left(a + d \frac{\cos i_1}{\alpha_1} \frac{\cos j_2}{\beta_2} \right) Hp^2 \right] D^{-1} \qquad \text{Equation B.1}$$

Where

$$a = \rho_2 \left(1 - 2\beta_2^2 p^2\right) - \rho_1 \left(1 - 2\beta_1^2 p^2\right) \qquad E = b \frac{\cos i_1}{\alpha_1} + c \frac{\cos i_2}{\alpha_2}$$

$$b = \rho_2 \left(1 - 2\beta_2^2 p^2\right) + 2\rho_1 \beta_1^2 p^2 \qquad F = b \frac{\cos j_1}{\beta_1} + c \frac{\cos j_2}{\beta_2}$$

$$c = \rho_1 \left(1 - 2\beta_1^2 p^2\right) + 2\rho_2 \beta_2^2 p^2 \qquad G = a - d \frac{\cos i_1}{\alpha_1} \frac{\cos j_2}{\beta_2}$$

$$d = 2\left(\rho_2 \beta_2^2 - \rho_1 \beta_1^2\right) \qquad H = a - d \frac{\cos i_2}{\alpha_2} \frac{\cos j_1}{\beta_1}$$

$$D = EF + GHp^2$$

And i_1 i_2 and j_2 are incident angle of P-wave, transmitted angle of P-wave and S-wave; α_1 α_2 and β_1 are incident P-wave velocity, transmitted P-wave velocity and transmitted S-wave velocity; p is the horizontal slowness or ray parameters.

For incident angle beyond critical angle, transmitted angle becomes complex number (Equation B.2), which accounts for phase rotated for supercritical angle reflections.

$$i_2 = \frac{\pi}{2} - i\cos^{-1}\left(\frac{\alpha_2}{\alpha_1}\sin i_1\right), \quad \frac{\alpha_2}{\alpha_1}\sin i_1 \geq 1 \qquad \text{Equation B.2}$$

Shuey (1985) gave the following equation after a modification in Aki & Richards (1980) approximation:

$$R_{pp}(\theta) = R_p + (A_o R_p + \frac{\Delta\sigma}{(1-\sigma)^2})\sin^2\theta + \frac{1}{2}\frac{\Delta V_p}{V_{Pa}}(\tan^2\theta - \sin^2\theta) \qquad \text{Equation B.3}$$

Where

R_p = normal incident reflection coefficient

V_{Pa} = average P-wave velocity of medium 1 and 2

σ = poison's ratio

θ = incient angle

$$A_o = B_o - 2(1+B_o)(\frac{1-2\sigma}{1-\sigma})$$

$$B_o = \frac{\Delta V_P}{V_{Pa}}/(\frac{\Delta V_P}{\Delta V_{Pa}} + \frac{\Delta\rho}{\Delta\rho_a})$$

This equation (Equation B.3) is often referred to as Shuey's formulation of the Aki and Richards approximation. A later equation is Shuey's two-term approximation (Equation B.4) and what is commonly referred to as Shuey's approximation:

$$R_{pp}(\theta) = R_p + B\sin^2\theta \qquad \text{Equation B.4}$$

Where

$$B = A_o R_p + \frac{\Delta\sigma}{(1-\sigma)^2}$$

The two-term of Shuey (1985) approximation becomes important at the intermediate angles (up to 30 degrees) where P-wave reflection co-efficient typically decreases approximately linearly with square of the sine of the angle.

Appendix C: NMO Correction and Stretch

C.1. NMO Correction

Dix (1955) gave the well-known hyperbolic two-way travel time equation as a function of zero-offset time t_o and offset x:

$$t = \sqrt{t_o^2 + \frac{x^2}{V^2(t_o)}} \qquad \text{Equation C.1}$$

Where t is the two-way travel time associated with a source-receiver separation (offset) x, t_o is the two-way zero-offset travel time (the time after normal move-out correction).

$V(t_o)$ is the NMO velocity, which can be estimated as the root-mean-square (rms) velocity for small offset approximation:

$$V_{rms} = \sqrt{\frac{\sum_{k=1}^{N} \Delta t_k V_k^2}{\sum_{k=1}^{N} \Delta t_k}} \qquad \text{Equation C.2}$$

And V_k is the interval velocity of the kth layer, Δt_k is the vertical two-way travel time to the kth layer.

For the area where bed are horizontally layered or gentle dipping at small offset, the expression (Equation C.3) originated with Dix (1955) could give fairly satisfied NMO correct time:

$$\Delta t_{NMO} = t - t_o = t - \sqrt{t^2 - \frac{x^2}{V^2(t_o)}} \qquad \text{Equation C.3}$$

C.2. NMO stretch

Consider a reflection event represented by a wavelet of dominant period T with an arrival time t at offset x. After normal-moveout correction, the dominant period becomes $T_o = T + \Delta T$. The moveout Equation C.1 is associated with the onset of the wavelet. Similarly, the moveout equation with the termination of the wavelet is expressed by

$$(t+T)^2 = (t_o + T + \Delta T)^2 + \frac{x^2}{v^2}$$ Equation C.4

Expand the terms on both sides:

$$t^2 + 2tT + T^2 = t_o^2 + 2t_o(T + \Delta T) + (T + \Delta T)^2 + \frac{x^2}{v^2}$$ Equation C.5

By making the substitution from Equation (C.1), we obtain

$$2\,tT + T^2 = 2\,t_o(T + \Delta T) + (T + \Delta T)^2$$ Equation C.6

Simplify and rearrange the terms

$$2(t - t_o)T = 2(t_o + T)\Delta T + \Delta T^2$$ Equation C.7

Now, ignore the second term on the right-hand side of the equation and observe that $\Delta t_{NMO} = t - t_o$ to obtain

$$\Delta t_{NMO} T = (t_o + T)\Delta T$$ Equation C.8

Assume that $t_o >> T$ and rearrange that terms to obtain a relationship for change in the period of the wavelet as a result of moveout correction

$$\frac{\Delta T}{T} = \frac{\Delta t_{NMO}}{t_o}$$ Equation C.9

Express Equation C.9 in terms of dominant frequency f of the wavelet with the relation

$$T = \frac{1}{f}$$ Equation C.10

And obtain

$$\Delta T = -\frac{1}{f^2}\Delta f$$ Equation C.11

Finally, combine Equation C.9 and Equation C.11 and to obtain the equation for the absolute value of frequency stretching:

$$\frac{\Delta f}{f} = \frac{\Delta t_{NMO}}{t_o}$$ Equation C.12

This is the same as Equation 2.1 in the main text, and usually 50 percent change of frequency is taken as threshold to determine the muting zone of the CMP gather.

Appendix D: Gassmann Fluid Substitution

Density of the water-saturated sand is estimated by Gardner's law (Gardner et al., 1974):

$$\rho = 0.23 V_p^{0.25} \qquad \text{Equation D.1}$$

As no shear velocity available here, V_s is estimated by Greenberg and Castagna (1992) V_p to Vs transforms (Equation D.2) for wet-sand and shale:

$$V_s = -0.856 + 0.804 V_p$$
$$V_s = -0.867 + 0.770 V_p \qquad \text{Equation D.2}$$

From the Gassmann's Equation, we can get dry frame moduli of sand K_{dry} from:

$$K_{dry} = \frac{K_b\left(\phi - 1 + K_{ma}/K_b - \phi K_{ma}/K_w\right)}{\phi + 1 - K_b/K_{ma} - \phi K_{ma}/K_w} \qquad \text{Equation D.3}$$

Where bulk modulus K_b is calculated by V_p, V_s and ρ of the water-saturated sand:

$$K_b = \rho\left(V_p^{\,2} - \frac{4}{3}V_s^{\,2}\right) \qquad \text{Equation D.4}$$

Then gas sand properties in the reservoir can be estimated by fluid substitution, the following Equation (D.5) is used for this purpose:

$$V_p = \sqrt{\left(K_{dry} + \frac{4}{3}\mu_{dry} + \frac{\left(1 - K_{dry}/K_{ma}\right)^2}{\left(1 - \phi - K_{dry}/K_{ma}\right)1/K_{ma} + \phi/K_{fl}}\right)\rho^{-1}} \qquad \text{Equation D.5}$$

$$V_s = \sqrt{\frac{\mu}{\rho}} \qquad \text{Equation D.6}$$

Here μ is the shear modulus of gas-saturated sand, which will not be changed with fluid content but with density:

$$\mu = \mu_{dry} = V_s^2 \rho \qquad \text{Equation D.7}$$

And K_{dry} and K_b are bulk modulus of dry rock frame and bulk rock; K_{fl} K_{ma} K_w ρ and ϕ are bulk modulus of substitute fluid (gas), matrix grains, original water, bulk rock density and porosity.